

# **Signal Enhancement in Magnetic Particle Imaging by a passive Dual Coil Resonator (pDCR)**

Signalverbesserung in der Magnetpartikel-Bildgebung durch einen passiven  
Doppelspulenresonator (pDCR)

**Jonas Philippss**

Bachelorarbeit in Physik  
vorgelegt der  
Fakultät für Mathematik, Informatik und Naturwissenschaften

angefertigt im Institut für  
**Experimentelle Molekulare Bildgebung**  
in der Arbeitsgruppe für  
**Physik der Molekularen Bildgebungssysteme**  
bei  
Dr.-Ing., Universitätsprofessor Volkmar Schulz  
und Zweitgutachter  
Dr. rer. nat., apl. Professor Oliver Pooth

Aachen, 3. Februar 2021



# Eidesstattliche Versicherung

## Statutory Declaration in Lieu of an Oath

Philipps, Jonas

377818

Name, Vorname/Last Name, First Name

Matrikelnummer (freiwillige Angabe)

Matriculation No. (optional)

Ich versichere hiermit an Eides Statt, dass ich die vorliegende Arbeit/Bachelorarbeit/  
Masterarbeit\* mit dem Titel

I hereby declare in lieu of an oath that I have completed the present paper/Bachelor thesis/Master thesis\* entitled

**Signal Enhancement in Magnetic Particle Imaging**

**by a passive Dual Coil Resonator (pDCR)**

selbstständig und ohne unzulässige fremde Hilfe (insbes. akademisches Ghostwriting) erbracht habe. Ich habe keine anderen als die angegebenen Quellen und Hilfsmittel benutzt. Für den Fall, dass die Arbeit zusätzlich auf einem Datenträger eingereicht wird, erkläre ich, dass die schriftliche und die elektronische Form vollständig übereinstimmen. Die Arbeit hat in gleicher oder ähnlicher Form noch keiner Prüfungsbehörde vorgelegen.

independently and without illegitimate assistance from third parties (such as academic ghostwriters). I have used no other than the specified sources and aids. In case that the thesis is additionally submitted in an electronic format, I declare that the written and electronic versions are fully identical. The thesis has not been submitted to any examination body in this, or similar, form.

Aachen, 03.02.2021

Ort, Datum/City, Date



Unterschrift/Signature

\*Nichtzutreffendes bitte streichen

\*Please delete as appropriate

**Belehrung:**

Official Notification:

**§ 156 StGB: Falsche Versicherung an Eides Statt**

Wer vor einer zur Abnahme einer Versicherung an Eides Statt zuständigen Behörde eine solche Versicherung falsch abgibt oder unter Berufung auf eine solche Versicherung falsch aussagt, wird mit Freiheitsstrafe bis zu drei Jahren oder mit Geldstrafe bestraft.

**Para. 156 StGB (German Criminal Code): False Statutory Declarations**

Whoever before a public authority competent to administer statutory declarations falsely makes such a declaration or falsely testifies while referring to such a declaration shall be liable to imprisonment not exceeding three years or a fine.

**§ 161 StGB: Fahrlässiger Falscheid; fahrlässige falsche Versicherung an Eides Statt**

(1) Wenn eine der in den §§ 154 bis 156 bezeichneten Handlungen aus Fahrlässigkeit begangen worden ist, so tritt Freiheitsstrafe bis zu einem Jahr oder Geldstrafe ein.

(2) Straflosigkeit tritt ein, wenn der Täter die falsche Angabe rechtzeitig berichtigt. Die Vorschriften des § 158 Abs. 2 und 3 gelten entsprechend.

**Para. 161 StGB (German Criminal Code): False Statutory Declarations Due to Negligence**

(1) If a person commits one of the offences listed in sections 154 through 156 negligently the penalty shall be imprisonment not exceeding one year or a fine.

(2) The offender shall be exempt from liability if he or she corrects their false testimony in time. The provisions of section 158 (2) and (3) shall apply accordingly.

Die vorstehende Belehrung habe ich zur Kenntnis genommen:

I have read and understood the above official notification:

Aachen, 03.02.2021

Ort, Datum/City, Date



Unterschrift/Signature

# Acknowledgments

First of all, I would like to thank my supervisor Dennis Pantke, who not only made this thesis possible, but also extensively proofread it. Thank you for the countless discussions and the always supportive advice.

Thanks also to Prof. Schulz, who provided some motivation with keen interest in my results, and also took over my supervision in the first weeks at the ExMI, sparking my deep curiosity for medical imaging. Prof. Pooth is also very much thanked for kindly taking on the role of second examiner.

In the last few months I have been able to really immerse myself in scientific work and gain incredible experience. I am grateful to the ExMI Institute and especially the PMI department for the exciting insights, discussions and support they have provided me with. I would especially like to thank Franziska, who helped with words and deeds.

Of course, I would also like to thank all my family and friends, without whom the road to my bachelor's degree would have been a lot more time-consuming and only a fraction as much fun. Especially, I would like to thank all of you who took on the burden of proofreading this thesis, I owe you one. Last but not least I want to thank my girlfriend, who thanks to all the lockdowns couldn't help but go through all the phases of this thesis and had to withstand me, I promise I'll compensate!

# Contents

<b>1</b>	<b>Introduction</b>	<b>1</b>
<b>2</b>	<b>Principles of MPI</b>	<b>3</b>
2.1	Superparamagnetic Iron Oxide Nanoparticles (SPIONs) . . . . .	3
2.2	Signal Generation . . . . .	4
2.3	Spatial Encoding . . . . .	7
2.4	Image Reconstruction . . . . .	9
2.5	Scanner Setup . . . . .	9
2.5.1	Signal Chain . . . . .	10
2.5.2	SNR and Threshold . . . . .	11
<b>3</b>	<b>Principles of the passive Dual Coil Resonator (pDCR)</b>	<b>13</b>
3.1	Motivation . . . . .	13
3.2	Basic Design of the pDCR . . . . .	14
3.2.1	Resonant Circuit . . . . .	15
3.3	Assembled pDCR Specifications . . . . .	16
<b>4</b>	<b>Influence of the pDCR on the MPI Signal Chain, SNR and Reconstructed Images</b>	<b>18</b>
4.1	Simulations . . . . .	18
4.1.1	Simulations in 1D . . . . .	19
4.1.2	Signal Simulations in 3D . . . . .	34
4.2	Measurements . . . . .	41
4.2.1	Scanner . . . . .	41
4.2.2	Tracer . . . . .	42
4.2.3	Phantoms . . . . .	42
4.2.4	Results and Discussion . . . . .	43
<b>5</b>	<b>Conclusion and Outlook</b>	<b>51</b>
	<b>List of Abbreviations</b>	<b>56</b>

<b>List of Figures</b>	<b>57</b>
<b>List of Tables</b>	<b>59</b>
<b>Bibliography</b>	<b>60</b>

# 1 | Introduction

Medical imaging is the process of visualizing the inside of the body. Most techniques are painless and non-invasive, meaning an incision in the skin or insertion of an instrument into the body is not necessary. Imaging techniques play a major role in providing diagnostic and therapeutic information and are an important tool for medical decision making. On their own, they can already save lives, as the current COVID-19 pandemic shows: The first crucial decisions were made based on computed tomography (CT) scans alone [1]. As part of medical technology, medical imaging also plays a crucial role in economic terms: Sales in the German medical technology industry amounted to around 33.4 billion euros in 2019, with almost 150,000 employees working in the sector [2].

While structural imaging techniques like computed tomography (CT) and magnetic resonance imaging (MRI) only display tissue and organs, functional imaging techniques like positron emission tomography (PET) and single-photon emission computed tomography (SPECT) aim to show physiological activities like blood flow or increased metabolism. A novel technique named magnetic particle imaging (MPI) is part of the latter group and will be the subject of this thesis. While existing imaging techniques are being optimized (e.g. multinuclear MRI [3] and photon-counting CT [4]) and combined (e.g. PET-MRI [5]), scientists are constantly coming up with new methods as well, one of which is the aforementioned MPI.

MPI was first introduced in 2005 by Gleich and Weizenecker [6] and has been part of interdisciplinary research ever since. The goal is the determination and imaging of the spatial distribution of superparamagnetic iron oxide nanoparticles (SPIONs) by stimulating them with external magnetic fields and taking advantage of their nonlinear magnetization behavior (for more details see section 2.1). MPI convinces with an outstanding temporal as well as good spatial resolution, allowing real-time imaging of biological processes. Furthermore, MPI is a quantitative imaging technique, meaning that one can directly infer the concentration of the particles from the measured signal. Also, the patient is not exposed to harmful radiation, as it is the case

with CT and PET. The different imaging techniques addressed are presented comparatively in more detail in Table 1.1.

	CT	MRI	PET	SPECT	MPI
Spatial resolution	0.5 mm	1 mm	4 mm	10 mm	<1 mm
Acquisition time	1 s	1 s-1 h	1 min	1 min	<0.1 s
Sensitivity	Low	Low	High	High	High
Quantifiability	Yes	No	Yes	Yes	Yes
Harmfulness	X-ray	Heating	$\beta/\gamma$ rad.	$\gamma$ rad.	Heating

Table 1.1: Comparison of the different imaging techniques (taken from [7]).

To benefit from the properties of MPI, especially in terms of spatial resolution, an excellent signal-to-noise ratio (SNR) must be achieved. This is especially important for the higher harmonics of the frequency spectrum (more details about this in chapter 3). To accomplish this goal, the passive dual coil resonator (pDCR) was proposed by Reinartz et al. [8]. The pDCR is a passive receive coil insert for the Bruker Preclinical MPI instrument (Bruker BioSpin MRI GmbH, Ettlingen, Germany), which enhances the sensitivity for a selected frequency band.

The goal of the submitted work is to further investigate the SNR gain of higher harmonics and the consequent gain in spatial resolution by using the pDCR. For this purpose, a simulation was implemented to analyze the enhancements in the frequency spectrum in more detail. Also, measurements at the preclinical Bruker MPI were performed with the aforementioned Bruker MPI scanner to investigate the improvements in spatial resolution and image quality and verify the findings of the simulations.

After this brief introduction, the basic principles of MPI are going to be introduced in chapter 2. Subsequently, chapter 3 will cover the pDCR functionalities. In chapter 4, the impact of the pDCR on the SNR and reconstructed images shall be evaluated, using simulations as well as measurements. Finally, in chapter 5, the findings are concluded and an outlook is given.

## 2 | Principles of MPI

In this chapter, the basic concepts of MPI are introduced. First, the SPI-ONs and their characteristics are illustrated, followed by the generation and encoding of the signal exhibited by the SPI-ONs and used for imaging. After that, the method of image reconstruction and the structure of an MPI scanner is briefly presented. If not cited otherwise, the content of this chapter has been written based on [7] and [9].

### 2.1 Superparamagnetic Iron Oxide Nanoparticles (SPI-ONs)

The goal of MPI is to create an image of a given spatial distribution of magnetic material. To achieve this, one takes advantage of the nonlinear magnetization response of small magnetic particles exposed to a time-varying magnetic field [6]. SPI-ONs are well suited for this purpose. These particles consist of a magnetic core and a magnetically neutral coating (Fig. 2.1). Superparamagnetic particles are ferromagnetic particles that are isolated enough from each other and small enough (typically core diameters are 1-100nm) so that their magnetic moments are independent [10].

When an external magnetic field  $H$  is applied, the magnetization response of the SPI-ONs  $M$  can be described via Eq. 2.1. The fields are of course vector functions, however, only their magnitude is used here.

$$M(H) = cm\mathcal{L}(\beta H) \quad (2.1)$$

where  $c$  is the particle concentration,  $m$  denotes the mean magnetic moment of the particles,  $\mathcal{L}$  is the Langevin function

$$\mathcal{L}(x) := \begin{cases} \coth(x) - \frac{1}{x} & x \neq 0 \\ 0 & x = 0 \end{cases} \quad (2.2)$$

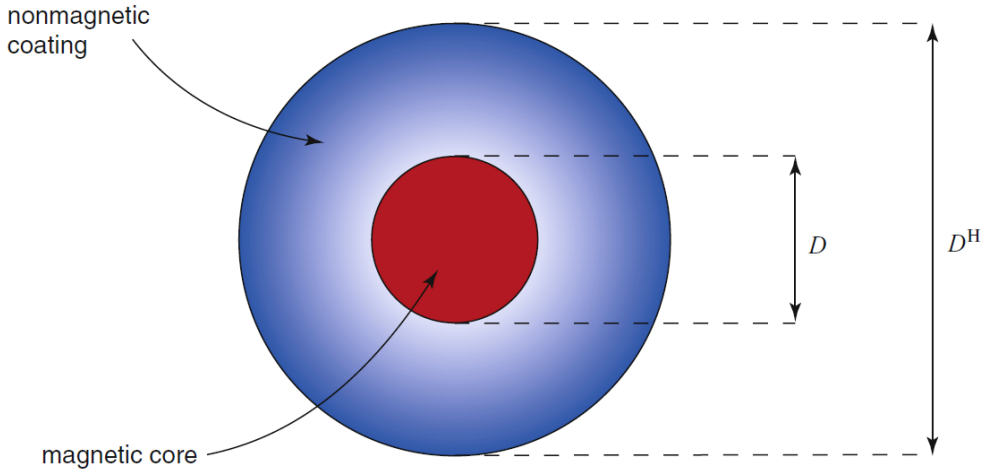


Figure 2.1: Schematic drawing of a SPION (taken from [7]).

and

$$\beta := \frac{\mu_0 m}{k_B T^P} \quad (2.3)$$

where  $k_B$  denotes the Boltzmann constant,  $T^P$  denotes the particle temperature,  $\mu_0$  is the vacuum permeability.

This nonlinear relation between  $M$  and  $H$  is shown in Fig. 2.2. One can identify the dynamic region, where changes in magnetization can be observed due to corresponding changes in the magnetic field. Outside this region, the magnetization is nearly constant and even large changes in the magnetic field do not result in considerable changes in magnetization since the particles are saturated. This means that all particles are already aligned with the magnetic field, resulting in the greatest possible magnetization. Therefore, this region is also called the saturation region.

## 2.2 Signal Generation

To continuously generate a response signal from the SPIONs, their magnetization is periodically driven into saturation by a homogeneous, time-varying magnetic field, called drive field (DF). The DF is generated by send coils and, to be more precise, is a mono-frequent sinusoidal field (for more details about the structure of an MPI scanner, respectively the arrangement of the different coils, see section 2.5). As the relation between the applied magnetic field and the magnetization is nonlinear (Fig. 2.2), the particles' magneti-

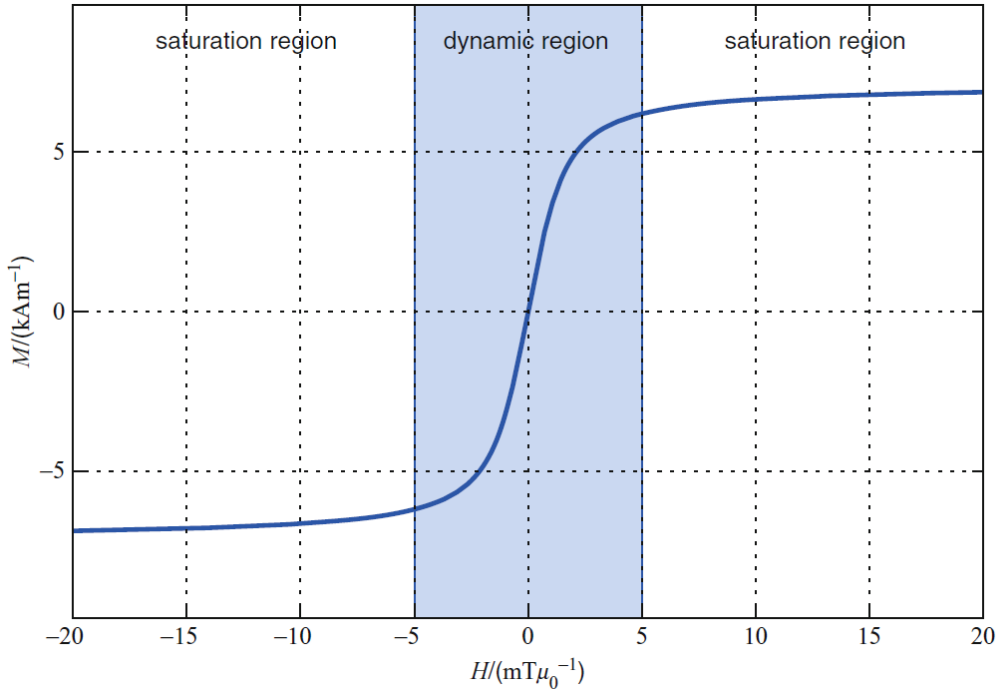


Figure 2.2: Nonlinear magnetization curve: Relation between the external magnetic field  $H$  and the magnetization of the particles  $M$  (taken from [7]).

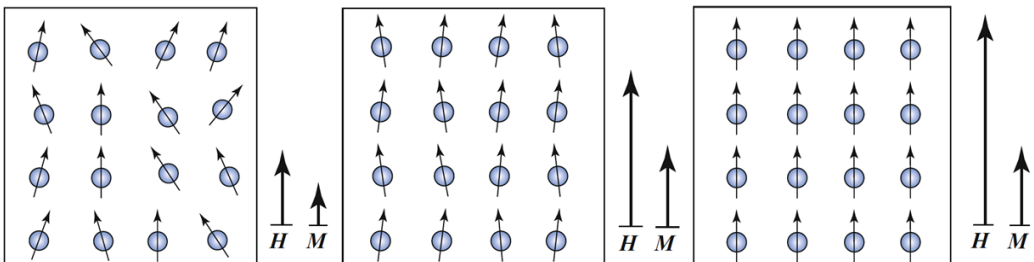


Figure 2.3: The particles' magnetic moments align along the magnetic field until saturation is reached (taken from [7]).

zation response on the excitation by the DF is not sinusoidal as well, but rather resembles a square wave (Fig. 2.4).

The particles' magnetization response is not measured directly instead, the voltage  $u(t)$  induced by the magnetization change in so-called receive coils is measured. The induced voltage can be described by Faraday's law of induction. In this case, the voltage induced in the receive coils by the

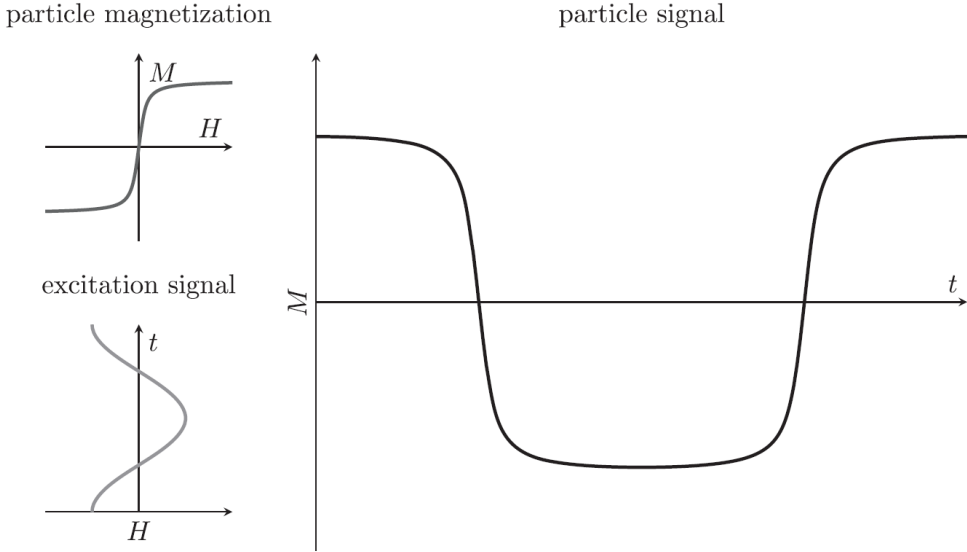


Figure 2.4: Counterclockwise: Particle magnetization (already seen in Fig. 2.2), excitation signal (DF) and resulting magnetization response of the SPI-ONs (taken from [9]).

particles' magnetization response can be described via

$$u(t) = -\frac{d}{dt} \int_V M(\mathbf{r}, t) \cdot p(\mathbf{r}) d^3 r, \quad (2.4)$$

where  $p(\mathbf{r})$  is the coil sensitivity.

Based on the magnetization curve shown in Fig. 2.4, the voltage curve shown in Fig. 2.5 is obtained by applying equation 2.4. The frequency spectrum of this voltage signal can be obtained by performing a Fourier transform. In the frequency spectrum, one cannot only observe the excitation frequency of the DF but also its higher harmonics, since the particles' magnetization response is not sinusoidal (Fig. 2.4), and therefore this is not the case for the voltage signal either.

It is important to note that not only the particles' magnetization response induces a voltage in the receive coils, but of course, also the DF itself, which provokes the response of the particles in the first case. More details can be found in the context of the signal chain in section 2.5.1.

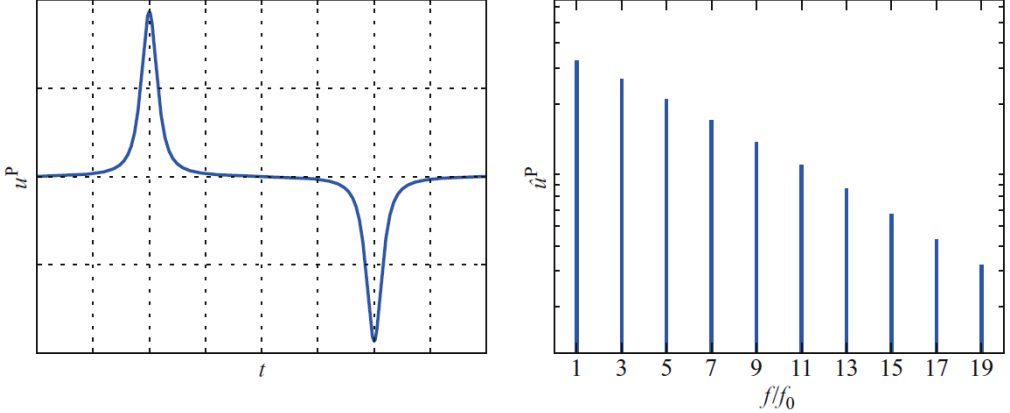


Figure 2.5: Induced particle signal in time and frequency space (taken from [7]).

## 2.3 Spatial Encoding

The excitation of all SPIONs in a volume with a homogeneous, time-varying DF alone only provides information on the mean concentration of SPIONs in the volume. To determine the desired spatial distribution, a so-called selection field (SF, Fig 2.6) is superimposed on the DF. The selection field is a magnetic gradient field that saturates nearly all SPIONs to prevent them from emitting a signal. Only SPIONs in the vicinity of the so-called field-free point (FFP), are excluded from this and are therefore able to exhibit a signal (Fig. 2.6). Mathematically, the SF can be written as

$$\mathbf{H}^S(\mathbf{r}) = \begin{pmatrix} G_x & 0 & 0 \\ 0 & G_y & 0 \\ 0 & 0 & G_z \end{pmatrix} \mathbf{r} = G \begin{pmatrix} -\frac{1}{2} & 0 & 0 \\ 0 & -\frac{1}{2} & 0 \\ 0 & 0 & 1 \end{pmatrix} \mathbf{r} \quad (2.5)$$

with  $G = G_z$  and the relation between the three gradient strengths

$$G_z = -2G_x = -2G_y. \quad (2.6)$$

These ratios meet Gauss's law for magnetism, which states that the magnetic field has divergence equal to zero

$$\nabla \cdot \mathbf{H} = 0. \quad (2.7)$$

By moving the FFP through a volume, a signal from all of the SPIONs at every position in space can be obtained. As taking a measurement at each position and moving the FFP in between the measurements takes a

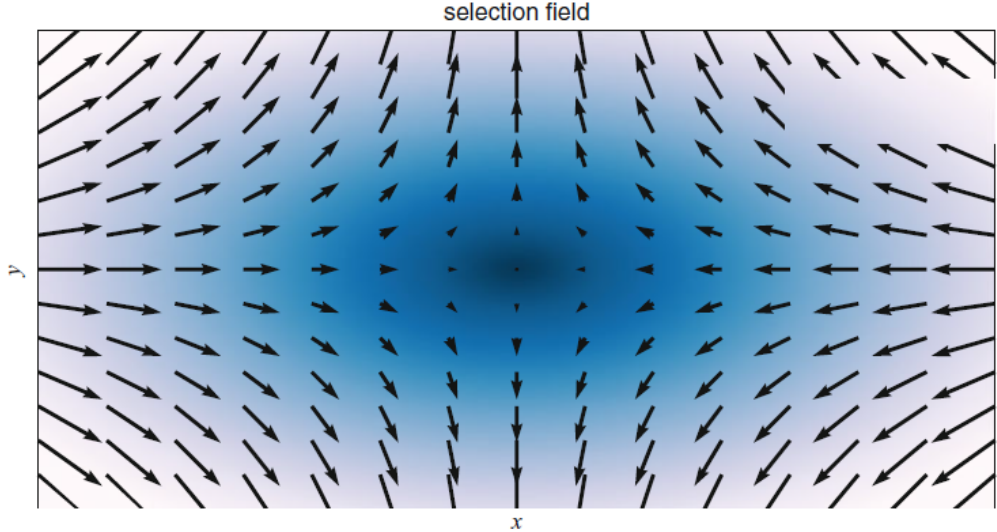


Figure 2.6: Selection field with field-free point (FFP) (taken from [7]).

long time, one chooses a much faster approach: Moving the FFP during the measurement through the volume to be imaged (also called field of view, FOV) and therefore receiving only one signal for the whole volume, instead of one signal per position. Usually, a Lissajous trajectory is used for this (Fig.2.7), but other trajectories are possible as well.

The area which the FFP can cover by following its trajectory is limited to a few centimeters and therefore is the size of the FOV (this limitation is only practical, not theoretical). To overcome this limitation and cover a larger volume, an additional magnetic field called focus field (FF) is superimposed. Simply put, this field moves the entire FOV through space.

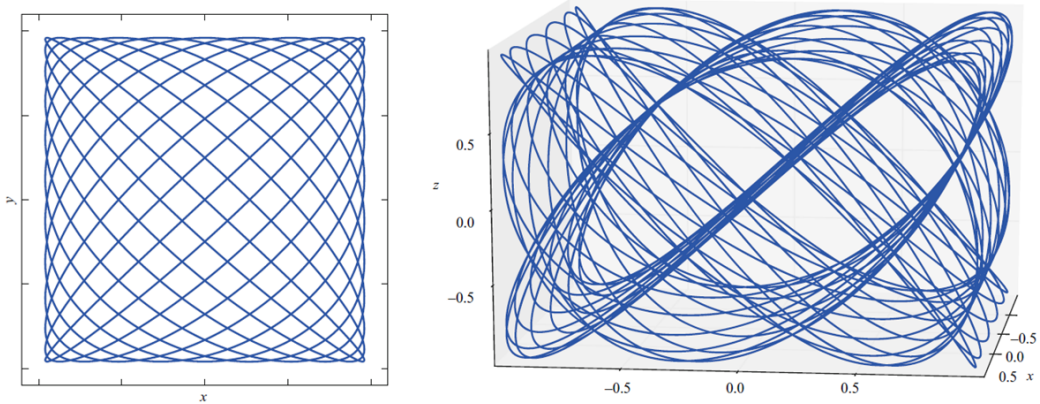


Figure 2.7: 2D and 3D Lissajous trajectory (taken from [7]).

## 2.4 Image Reconstruction

To obtain the particle concentration of interest from the voltage signal induced in the receive coils, one has to solve an inverse problem, referred to as reconstruction. It holds:

$$\mathbf{Sc} = \hat{\mathbf{u}} \quad (2.8)$$

with  $\mathbf{S} \in \mathbb{C}^{M \times N}$  the system matrix (SM),  $\mathbf{c} \in \mathbb{C}^N$  the particle concentration vector and  $\hat{\mathbf{u}} \in \mathbb{C}^M$  the (ideal, noise free) measurement vector containing the Fourier coefficient of the induced voltage's signal spectrum. In order to deduce the concentration from the voltage, the SM must be determined. This determination is an essential part of the reconstruction.

The SM describes the spectra of a delta sample being placed at every position in the FOV. These volume elements represented by these positions are referred to as voxels. The SM consists of  $N$  rows for each observable frequency of the spectrum and  $M$  columns for every position in the FOV. Usually, the rows of the matrix are reduced to the harmonics of the spectra, as it is also the case in the simulation which was implemented in the course of this work.

The SM can either be obtained by actual measurements, recording the spectra of the delta sample at every position [6], or by modeling all processes, including the signal chain (section 2.5.1) [11]. The former, called measurement-based system function approach, allows higher resolutions and larger FOVs, while the second, called model-based approach, ensures a much shorter computation time. As for the former approach, one does not need any information about the MPI system (particle and scanner characteristics) and also does not need to apply model simplifications. This approach has been used in most MPI publications and was also used for the measurements that are part of this thesis.

To solve the system of linear equations (Eq. 2.8), the widespread Kaczmarz method, an iterative solver for systems of linear equations [12], is used in this work. In principle, each linear equation of the system is interpreted as a hyperplane in the  $N$ -dimensional solution space and in each iteration, the current estimate of the solution is projected onto this hyperplane.

## 2.5 Scanner Setup

A common MPI scanner, which applies the DF in all three spatial directions, is built around a cylindrical bore and consists of the following components (Fig. 2.8):

- combined selection and focus field coils (red): generate the FFP and apply the focus field
- focus field coils (orange): apply the FF in orthogonal directions
- drive field coils (green): generate the DF for excitation in every direction
- receive coils (blue): pick up the particles' magnetization response in every direction

The presented passive coil insert (pDCR), the principles of which are described below, fits exactly into the scanner bore and will enhance the signal received in the receive coil in  $x$ -direction.

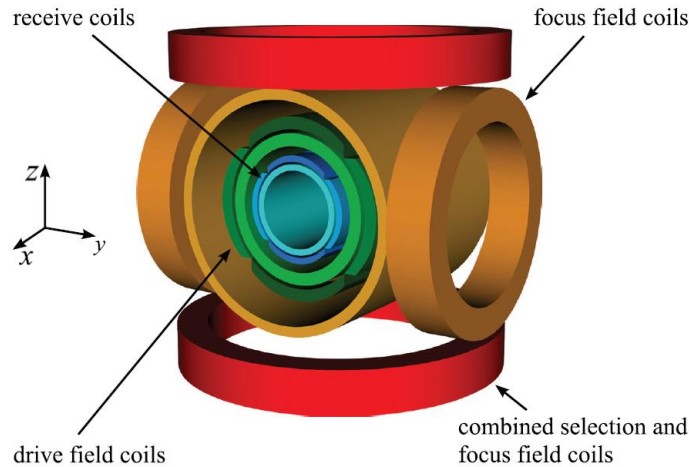


Figure 2.8: MPI scanner setup (taken from [9]).

### 2.5.1 Signal Chain

As mentioned at the end of section 2.2, not only the SPIONs' magnetization response induces a voltage in the receive coils but also the dynamic magnetic DF generated by the transmit coils.

The amplitude of the signal directly induced by the DF is several orders of magnitude greater than the voltage induced by the particles and thus, the DF feed-through drowns out the particle signal. Therefore, the induced DF signal must be filtered out. This is accomplished by analog band-stop filters, which are part of the signal chain shown in Fig. 2.9.

The send coils are fed by a signal generator, followed by a band-pass filter, only letting the wanted excitation frequency for the DF pass. The

DF then excites the SPIONs, provoking a magnetization response. As just explained, this signal picked up by the receive coils contains not only the induced particle signal (green) but also the excitation signal (red) (left plot in Fig. 2.9). The frequency of the excitation signal is filtered out by a band-stop filter (center plot). This also filters out the particle signal at this frequency (i.e. the particles' signal's first harmonic), so one only uses the remaining harmonics of the signal (plot on the right). The remaining signal is then amplified and digitized.

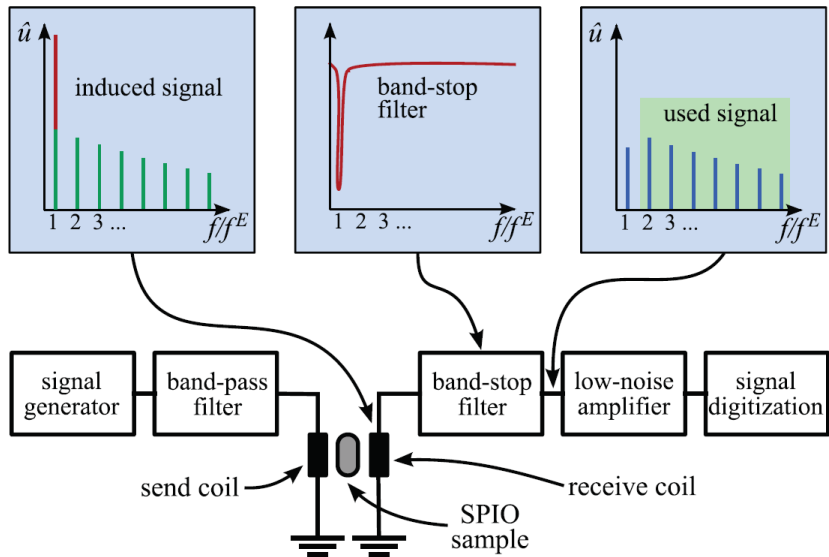


Figure 2.9: MPI Scanner signal chain (taken from [9]).

### 2.5.2 SNR and Threshold

There are numerous ways to define the SNR, in this work the following is used. The mean values of the background spectra ( $BG$ ) are subtracted from the mean values of the spectra ( $S$ ) yielding the mean values of the background-corrected spectra. These are then divided by the standard deviation of the background spectra ( $\sigma(BG)$ )

$$SNR = \frac{S - BG}{\sigma(BG)}. \quad (2.9)$$

The standard deviation is the square root of the average of the squared deviations from the mean and is implemented in Python as part of the NumPy library as

```
std = sqrt(mean(abs(x - x.mean())**2)).
```

Note that the absolute value is taken before squaring, yielding an always real and non-negative result [13].

In the following, the SNR of the whole SM will also play a role. For the calculation of this, the individual SNRs of each position are calculated and the mean of their absolutes is taken.

# 3 | Principles of the passive Dual Coil Resonator (pDCR)

The following pages will outline the working principles of the pDCR. First, the motivation will be presented, then the basic concepts and design ideas will be discussed and finally, the precise design of the pDCR used for this work will be described.

## 3.1 Motivation

One of the biggest challenges in MPI is to achieve a good SNR, especially for higher harmonics. The intention behind this is that as many harmonics of the induced particle signal as possible, which drop in intensity at higher frequencies and then disappear in the noise floor, should be usable for image reconstruction to reach a better spatial resolution (Fig. 2.5 and Fig. 3.2) [14]. To enhance the harmonics at higher frequencies, one aims to increase the inductive coupling between the particles and the receive coils at higher harmonics. You find more on how this is accomplished in the next section.

To highlight the importance of high-frequency components concerning spatial resolution, in the following, the Fourier transform of the square wave is shown. The square wave is defined by:

$$f(t) := \begin{cases} 1 & t \in [0, \pi) \\ -1 & t \in [\pi, 2\pi) \end{cases} \quad (3.1)$$

and can be approximated by a Fourier series as follows:

$$f(t) \sim \frac{a_0}{2} + \sum_{k=1}^n (a_k \cos(kt) + b_k \sin(kt)) \quad (3.2)$$

with the Fourier coefficients  $a_k$  and  $b_k$ . In Fig. 3.1, partial sums of the Fourier series of the square wave are plotted with different numbers of elements. One can directly see, that the more elements of the Fourier series

are used, the more the series resembles the original function. Analogously, a better resolution in MPI results if more harmonics (which correspond to the elements of the Fourier series in the example) can be used for reconstruction.

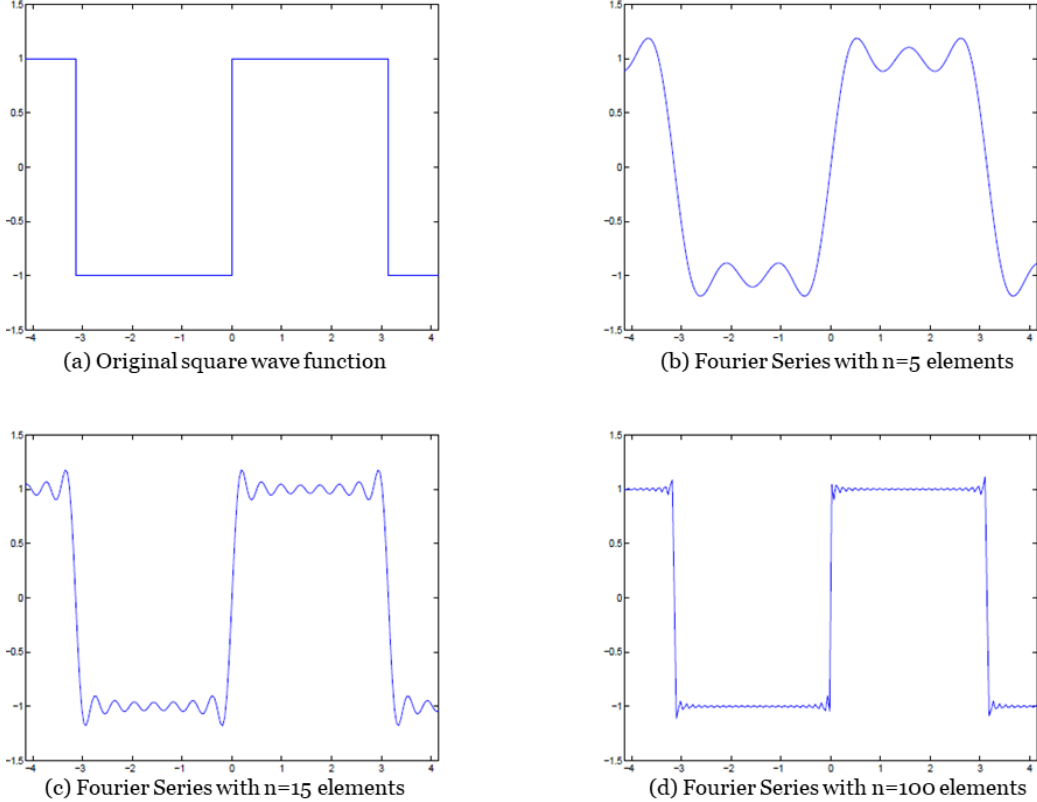


Figure 3.1: Original square wave function and partial sums of the Fourier series for  $n=\{5,15,100\}$  elements.

### 3.2 Basic Design of the pDCR

As the name suggests, the pDCR, which consists of two coaxial coils, is passive because it does not have a voltage source and also no electrical connection to the rest of the MPI scanner system. The pDCR represents a resonant circuit and therefore also includes a capacitor (a brief explanation of the operation principle of an electric resonant circuit follows in the next section).

The pDCR picks up the particles' magnetization response mainly with its interior coil (right coil in Fig. 3.2). It then sends out the received signal

with its exterior coil (left coil in Fig. 3.2) but enhanced in the range of its resonant frequency. This output is then picked up by the scanner's receive coils. There will be coupling between all the different coils of the scanner and the pDCR, however, the described process will dominate.

Mutual induction is also relevant in this context. A change in current in one inductor induces a voltage in another nearby inductor

$$U_2 = M_{21} \cdot \frac{dI_1}{dt}. \quad (3.3)$$

The mutual inductance  $M_{ij}$  is thereby a measure of the coupling between two inductors

$$M_{12} = M_{21} = \frac{\mu_0}{4\pi} \int_{s_1} \int_{s_2} \frac{ds_1 \cdot ds_2}{r_{12}} \quad (3.4)$$

with the line elements of the respective inductors  $s$  and their distance  $r_{12}$  [15].

The pDCR, i.e. the resonant circuit, is tuned to a frequency near the frequency at which the harmonics of the signal disappear into the noise floor and thus serves its function as mentioned above (Fig. 3.2).

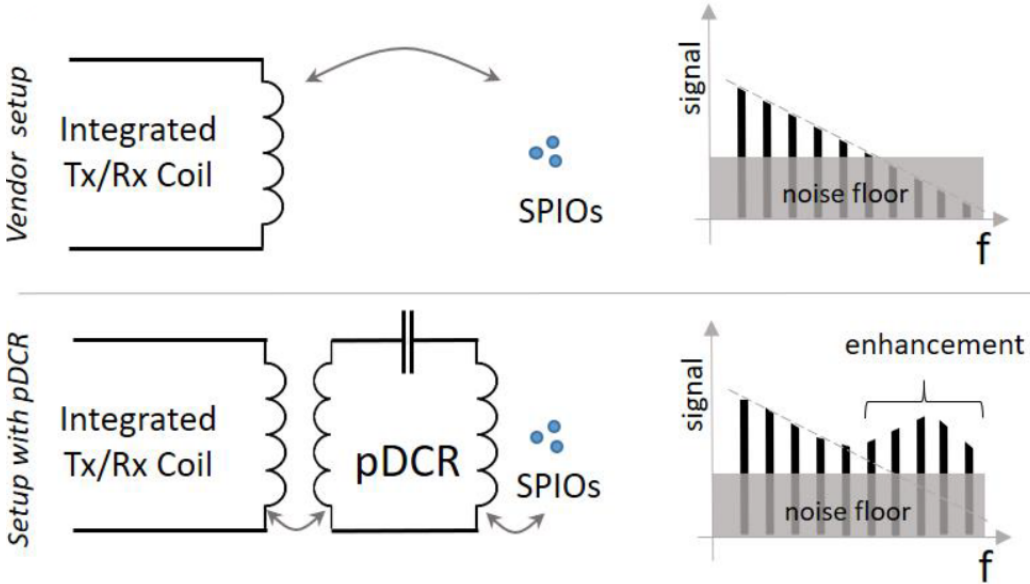


Figure 3.2: Schematics of the pDCR functionality (taken from [8]).

### 3.2.1 Resonant Circuit

A resonant circuit is an electrical circuit consisting of an inductor and a capacitor. Periodically, the capacitor, which stores the electrical potential

energy  $W_E = 1/2 \cdot CU^2$  (with  $C$  the capacitance and  $U$  the voltage), is discharged via the coil. The current  $I = dQ/dt$  flowing in the process generates a magnetic field in the coil with the magnetic energy  $W_B = 1/2 \cdot LI^2$  (with  $L$  the inductance and  $I$  the current). Due to Lenz's law, a voltage is induced, which charges the capacitor and the cycle starts all over again [15]. The circuit stores energy oscillating at the resonant frequency

$$\omega_0 = \frac{1}{\sqrt{LC}}. \quad (3.5)$$

If the ohmic resistance is included, the resonant frequency is calculated via

$$\omega_R = \sqrt{\frac{1}{LC} - \frac{R^2}{4L^2}}. \quad (3.6)$$

### 3.3 Assembled pDCR Specifications

The pDCR, which was already designed and constructed prior to the work presented here, consists of two coaxial cylinders with diameters of 50 mm and 110 mm (Fig. 3.3). On each cylinder, 31 turns of a 1.5 mm thick insulated stranded wire were continuously wound (and thus form the coils). The inductance of the coils combined can be measured with a network analyzer at approx. 610 kHz to approx. 210  $\mu$ H. The coils are electrically connected by 7 capacitors (630 V, 2200 pF, 10% tolerance; WIMA GmbH & Co. KG, Mannheim, Germany). The capacitors are connected in series, which results in a total capacitance of 0.314 nF. With Eq. 3.5, this results in a resonant frequency of 620 kHz. The resonant frequency was previously measured to approx. 608 kHz. The difference can be explained by the neglected ohmic resistance and possible uncertainties of measurement.

This design fits perfectly into the Bruker Preclinical MPI instrument and is placed in the center of the bore to achieve the best coupling between the outer coil of the pDCR and the  $x$ -receive coil of the Bruker scanner. A detailed sketch can be found in the appendix, and a photograph can be seen in Fig. 3.3.



Figure 3.3: Photograph of the assembled pDCR in front of the Bruker MPI bore.

# 4 | Influence of the pDCR on the MPI Signal Chain, SNR and Reconstructed Images

The main task of this thesis is to analyze the changes in the signal spectrum and the expected subsequent improvements of spatial resolution, which can be obtained by using the pDCR. To optimize the resonance frequency with respect to the image quality improvement, a simulation program was written in Python [16]. Additionally, measurements were carried out with the Bruker Preclinical MPI instrument using the pDCR design characterized in section 3.3.

## 4.1 Simulations

The spectrum of the voltage signal induced in the receive coils by the SPIONs was simulated. The influence of the pDCR on the harmonics' magnitude and phase of this spectrum and thus, on the image quality is to be investigated.

The developed simulation program builds upon the existing program by the former master student Nils Holle [17], which was implemented during his master thesis [18] at the Institute for Experimental Molecular Imaging (ExMI) at the Department of Physics of Molecular Imaging Systems (PMI) and can be found at [16]. Holle's program is written in Python and accomplishes the simulation of the magnetization spectrum emitted by a given particle distribution as well as the SM. The simulation is also capable of taking care of the associated image reconstruction. Several particle properties, as well as scanner related measurement properties, are included. Simply put, a SM is simulated using the Langevin theory for describing the magnetic behavior of the SPIONs. The signal acquisition is accomplished via a Lissajous

trajectory. The SM elements are calculated via:

$$\mathbf{S}_{ij} = i\omega_i \mu_0 m \mathbf{R} \frac{V}{N} \mathcal{F}[\mathcal{L}(\mathbf{r}(t) - \mathbf{x}_j)](\omega_i) \cdot \hat{\Gamma}(\omega_i). \quad (4.1)$$

where  $\mathbf{S}_{ij}$  are the entries of the SM with  $i$  indexing the frequencies of the spectra and  $j$  the positions of the FOV. The matrix  $\mathbf{R}$  denotes the receive coils sensitivity and  $\frac{V}{N}$  is the volume of one voxel.  $\mathcal{F}[\mathcal{L}(\mathbf{r}(t) - \mathbf{x}_j)](\omega_i)$  is the  $i$ -th coefficient of the Fourier transform of  $\mathcal{L}(x)$ . The factor  $\hat{\Gamma}(\omega_i)$  describes the particles' relaxation behavior. For more details, please refer to the thesis of Holle [18]. The simulated SM is then multiplied by a given particle concentration vector yielding the signal spectrum of the respective particle distribution (Eq. 2.8). For image reconstruction, the Kaczmarz method is used [12]. For further details please refer to Holle's thesis and code. The use of this program seems reasonable as its data output has already been successfully reused in other theses [19].

In addition, the developed program uses measurements of the receive chain already made in advance by Ph.D. student Dennis Pantke at the in-house developed multi-frequency (mf) MPI [20].

The simulation program was written for 1D DF as it is implemented in the mf MPI as well as for 3D DF as it can be applied in the preclinical Bruker MPI. [21].

#### 4.1.1 Simulations in 1D

##### Frequency Spectrum

The particles' magnetization signal generated for the magnetization response to a 1D DF was simulated with the abovementioned program using the properties from Tab. 4.1. A SM FOV with a length of 15 mm was simulated, which is divided into 15 positions yielding 1 mm distance between the SM positions. A delta sample is placed in the central position. With a SF gradient of  $G_{SF} = 2.5$  T/m and a DF amplitude of  $A_{DF} = 14$  mT, the  $FOV_{DF}$  can be calculated via the following equation to 11.2 mm.

$$FOV_{DF} = \frac{2A_{DF}}{G_{SF}} \quad (4.2)$$

Thus, the FOV shows an overscan compared to the  $FOV_{DF}$ . The concept of overscanning allows reducing the reconstruction errors (or artifacts) induced by SPIONs outside of the  $FOV_{DF}$ , while they are still contributing to the measured signal [22].

Signal generation parameters	
DF frequency [kHz]	25
DF amplitude [mT]	14
SF gradient [T/m]	2.5
saturation field strength [mT/ $\mu_0$ ]	1.6
relaxation time $\tau$ [ $\mu$ s]	1/6
Reconstruction parameters	
number of iterations	30
regularization	5e-5
SM parameters	
number of positions	15
FOV [mm]	15

Table 4.1: Signal generation parameters and reconstruction parameters in the 1D simulation. For reconstruction the Kaczmarz algorithm was used.

With the aforementioned scanner and particle properties and the described delta sample in the center of the FOV, the simulation is carried out. The results are shown in Fig. 4.1.

- At the top one can see the magnetization spectrum of the delta sample, which is put out by the simulation program. All further simulations, which were carried out in the context of this thesis, proceed from this point. Note that only every second harmonic of the spectrum can be seen, since every other vanishes due to the central positioning of the delta sample.
- Beneath that, the respective particle magnetization signal calculated by taking the inverse Fourier transform of the simulated magnetization spectrum can be observed.
- In the second plot from the bottom, the voltage induced in the receive coils, calculated following Eq. (2.4), is shown. Note that the sensitivity  $p$  is chosen to be 1, as the coil sensitivity is already included in the transfer function, which will be applied later on.
- In the bottom plot, the respective spectrum of this voltage signal, calculated by taking the Fourier transform, can be seen. Note that the pDCR is only about to become relevant and its influence has not played a role yet.

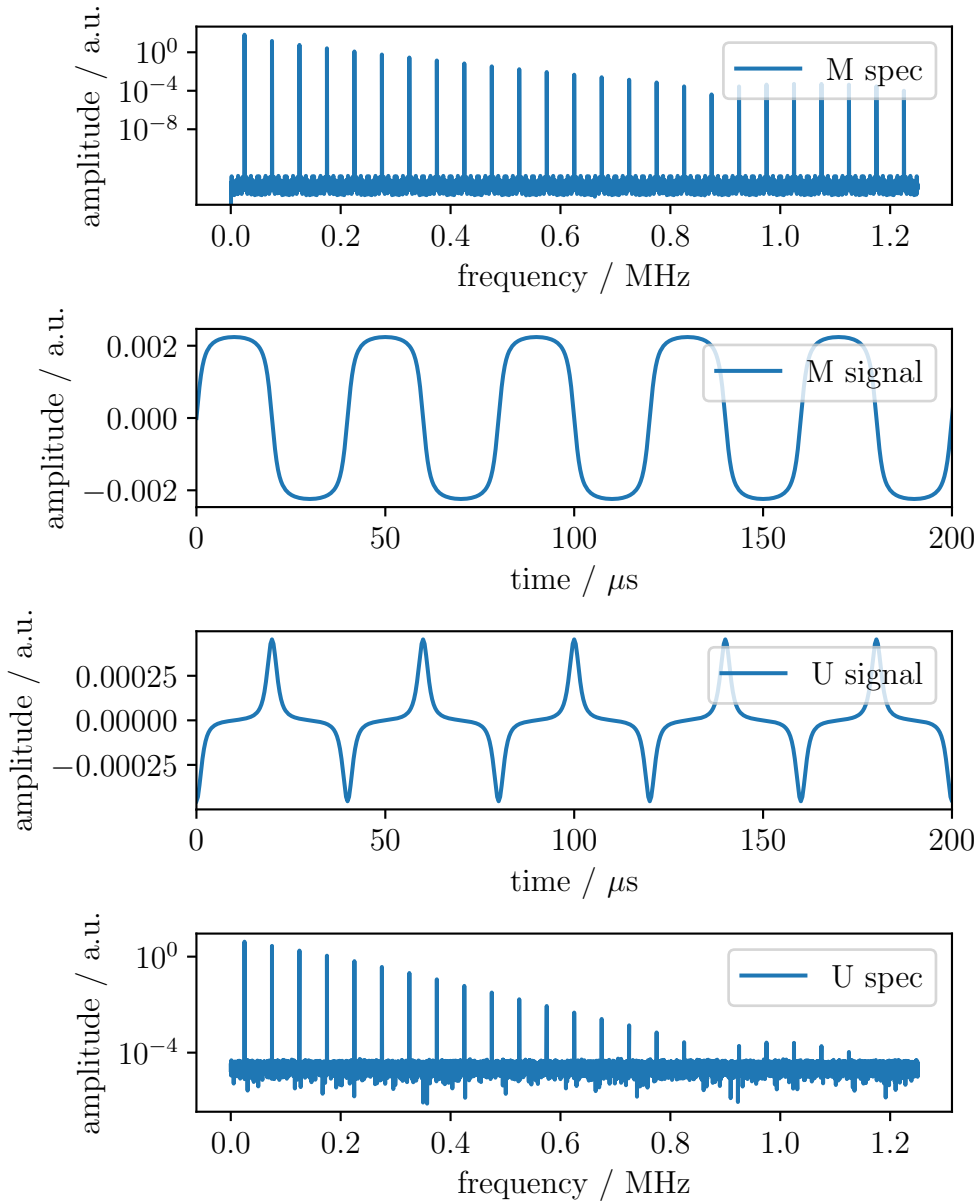


Figure 4.1: Simulation results for the magnetization response to a 1D DF. From top to bottom: particles' magnetization response in frequency space, in time space, voltage induced in the receive coils in time space, in frequency space.

## Receive Chain and Signal Tuning

The simulated voltage signal, which can be seen in the second plot from below in Fig. 4.1, represents the signal that is induced in the receive coils assuming that only particles and receive coils exist and the pDCR is not in use. In reality, the magnetic fields generated by the send coils will directly induce a voltage signal in the receive coils as well, but since this is filtered out and not used for reconstruction anyway (Fig. 2.9), it will be neglected in the simulation process. Since the voltage signal itself is not used directly but must first pass through the receive chain, the transmission through the receive chain needs to be considered. A simulation of every part of the receive chain, as well as the exact interactions of the pDCR with the magnetic particles, and the scanner elements, would be unnecessarily complicated instead, the transfer function of the whole receive chain was measured, once with and once without the pDCR. The receive chain was measured with the help of a network analyzer and a small transmit coil. The output of the network analyzer was connected to the transmit coil, which was placed inside the MPI bore. The output signal of the low-noise-amplifier (LNA) was picked off with the the network analyzer input. The measured transfer function represents every part of the receive chain including the pDCR when it is in use. The function includes all changes that the signal induced in the receive coils goes through (i.e. filtering, damping, etc.) before it is finally put out as a digitized signal by the scanner electronics for further processing (e.g. image reconstruction). The impact of the pDCR on the voltage spectrum is fully described by the transfer function.

The measured receive chain function can be seen in Fig. 4.2. As expected, when the pDCR is inserted the transfer function is increased at high frequencies between approx. 0.4 MHz and 1.1 MHz, which means an increased receive sensitivity in the respective frequency range. The peak of the pDCR transfer function can be found at 0.694 MHz and is called pDCR peak from now on. In comparison with section 3.3, it is noticeable that this is not the exact resonant frequency of the pDCR itself. The reason for the shift is most likely the previously neglected coupling of pDCR with the transmitting and receiving coils and other scanner components. Notice that the  $x$ -axis is shown on a logarithmic scale, so one can better observe the sophisticated course of the transfer function at the frequency range of about 20-30 kHz. This part impressively shows the effect of the band-stop filter. The excitation frequency of 25kHz is dampened by approximately 125 dB. Also, the transfer function covers the frequency range from 10 kHz to 2 MHz.

The goal is to determine the processed and refined output of the signal chain from the simulated voltage spectrum induced in the receive coils (see

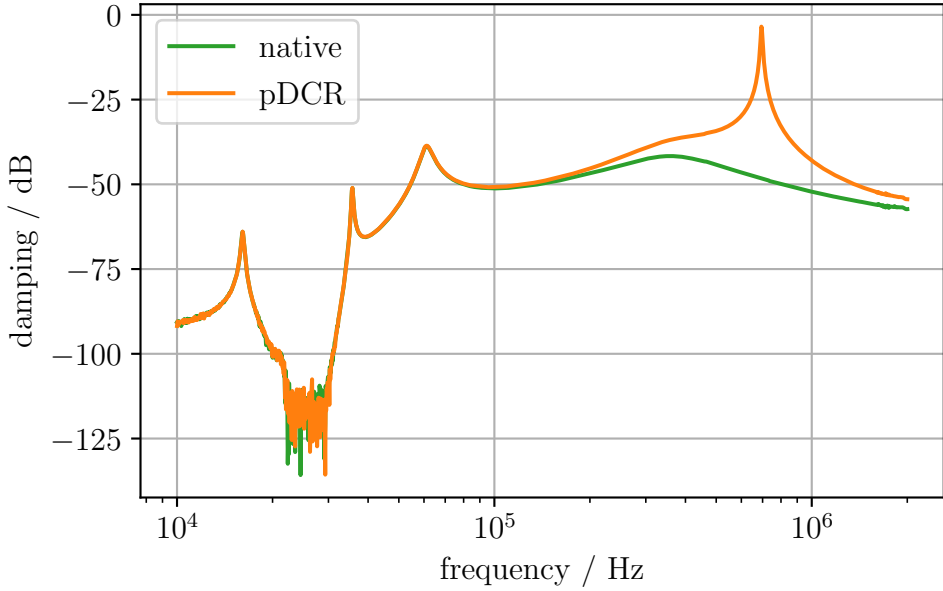


Figure 4.2: Transfer function for native and pDCR setup, logarithmic scale on  $x$ -axis.

the bottom plot in Fig. 4.14). To do this, one has to simply multiply the voltage spectrum with the transfer function. As the simulated spectrum consists of more data points than the transfer function, one has to interpolate at the missing frequencies.

The result of the multiplication can be seen in Fig. 4.3. Notice that the mean of 500 simulated spectra is shown. The impact of the pDCR becomes visible, more details on that can be found in the next section. In the following, data simulated for the native scanner setup will be plotted in green, while data simulated for the scanner setup with the pDCR will be plotted in orange.

### Noise Modeling

Gaussian noise was added at several points during the simulation. First in the voltage induced in the receive coil, second in the voltage induced in the pDCR, and third at the end of the signal chain. The amplitudes of the noise contributions were always chosen in such a way that the resulting noise floor resembled that in the real measurements as closely as possible. Thus, the shape of the SNR is as realistic as possible and the findings from the simulation can be well transferred to real measurements and real SNRs.

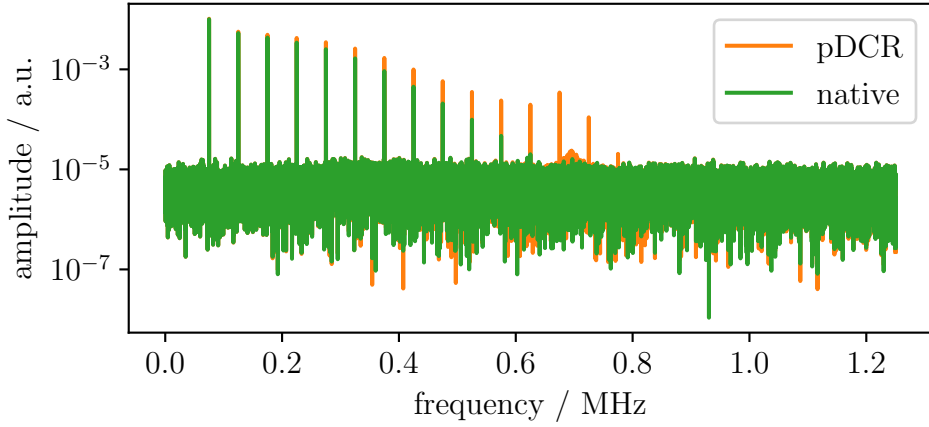


Figure 4.3: 1D simulation signal chain output: magnetization spectrum tuned with the transfer function (mean of 500 simulated spectra).

### SNR and Image Reconstruction

The SNR of the tuned voltage signal spectrum is calculated over 500 simulated spectra (and according to Eq. 2.9). The resulting SNR can be observed in Fig. 4.4. The desired SNR enhancement at higher harmonics with the pDCR is visible. While the harmonics are disappearing in the noise floor at approx. 0.62 MHz with the use of the native setup, the pDCR allows detecting harmonics up to approx. 0.78 MHz. Besides, the pDCR enhances all harmonics almost from the beginning. The real impact of the pDCR becomes visible from 0.6 MHz on, when the harmonics are strongly amplified compared to the native signal and then even increase in amplitude and form a peak.

Compared to the actual measurements that will follow at the end of this thesis, it can be pointed out that the form of the pDCR peak and the noise level are well chosen and are very similar to the measurements. Especially the point at which the harmonics are disappearing into the noise floor is well met.

Coming back to the simulation for a moment. The program simulates the SM which is then multiplied by the particle concentration vector yielding the signal spectrum. It is important to note here, that it is not the voltage induced in the receive coils that is simulated, but the magnetization of the particles. The conversion steps, which are performed with the signal spectrum to obtain the induced voltage and its spectrum that are described and shown above are performed analogously with the entire SM (i.e. with each spectrum included in the SM). This yields the voltage signal spectrum as well

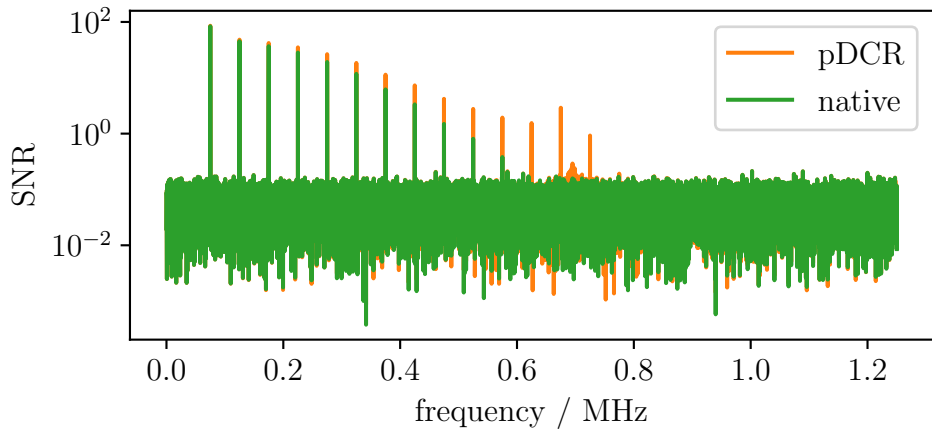


Figure 4.4: SNR in 1D with 500 repetitions.

as the analog SM (no longer containing the magnetization spectra, but the voltage spectra), which can now be used to perform the image reconstruction according to Eq. 2.8. As mentioned, the simulation program takes care of the reconstruction. The so-called dax function, a Kaczmarz solver ([23] and [17]), maps two arrays, one containing the signal spectrum and another the respective SM, to an array representing the reconstructed image.

As described in section 2.5.2, the SNR of the whole SM shall be obtained to define a threshold therein. So only harmonics with an amplitude in the SNR of the SM that lies above a specific threshold are used for reconstruction. For this purpose, the SNR of every spectrum in the SM is calculated and the mean of the absolutes of these SNRs is taken. The resulting mean SNR of the SM can be observed in Fig. 4.5.

Since the threshold is chosen by the experimenter in actual measurements, different thresholds are implemented and it is investigated, how many harmonics in the SM SNR lie above the respective threshold in each case. Thresholds between 0.3 and 8 were implemented and the number of harmonics above the respective thresholds is shown comparatively in Fig. 4.6. The ratio of harmonics above the threshold of pDCR to native is shown in Fig. 4.7

One can see that for all thresholds, the pDCR amplifies harmonics with former low amplitude so that their amplitude lies now above the respective thresholds. Thus, more harmonics can be used for image reconstruction. This is expected to result in better spatial resolution, since not only more but mainly more harmonics with higher frequencies are used for the reconstruction. One recalls that this is the inherent goal of pDCR. The ratio of pDCR to native in terms of numbers of harmonics above the threshold peaks

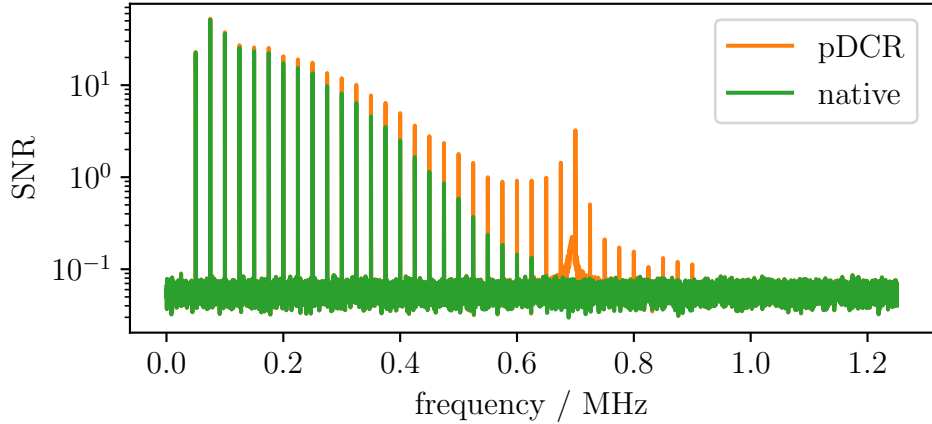


Figure 4.5: SNR of SM in 1D with 500 repetitions.

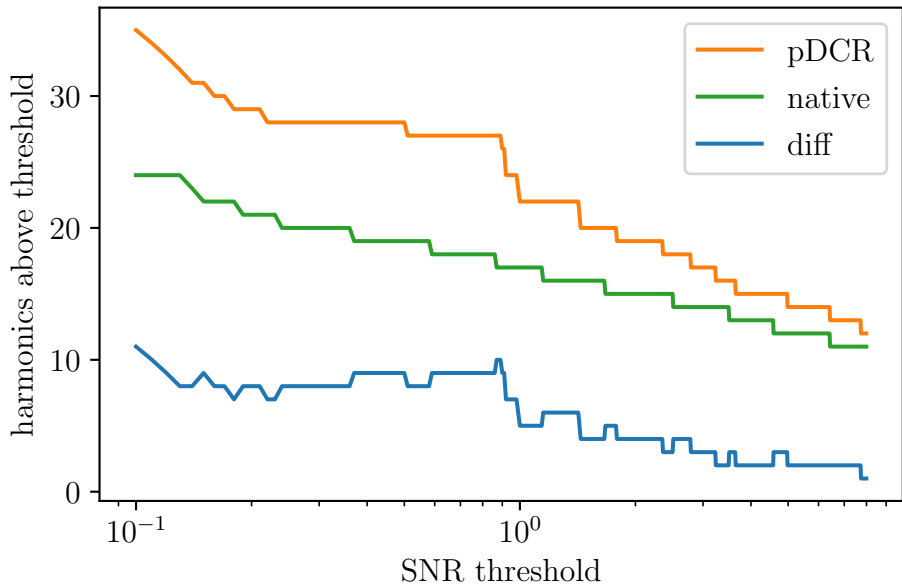


Figure 4.6: Comparison and difference between pDCR and native of number of harmonics above threshold.  $x$ -axis on logarithmic scale.

at 1 with 1.6 and then drops nearly to 1 for high thresholds.

To be able to examine the changes in image quality in more detail, reconstructions are performed with certain prominent thresholds in use. It was focused on how the differences in image quality change starting from a quite low threshold, where most of the harmonics lie above the threshold, via a threshold at which the pDCR peak lies just above it, to a threshold, where

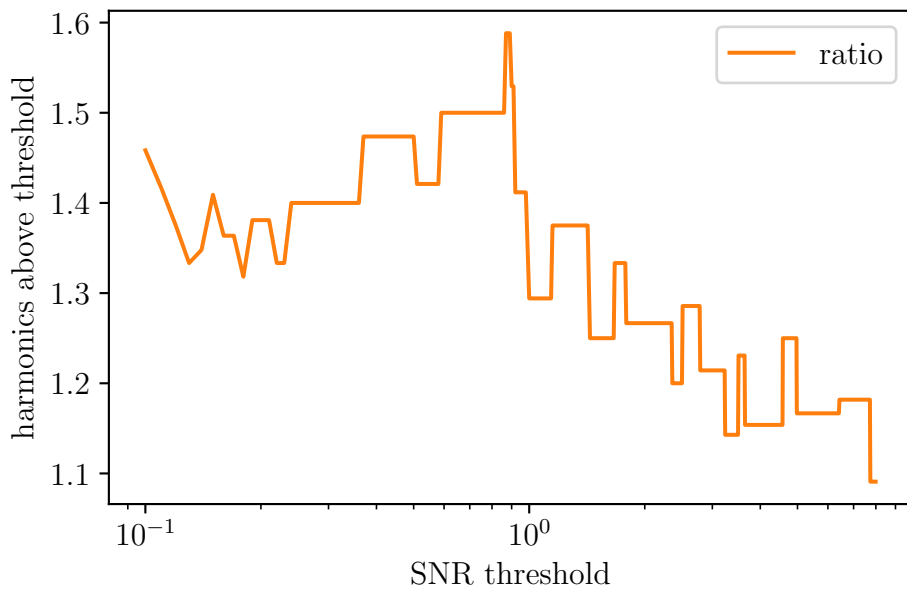
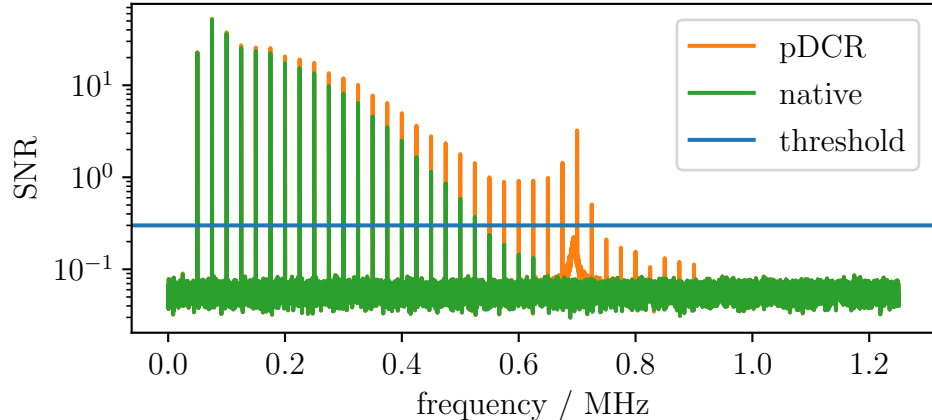


Figure 4.7: Ratio of pDCR to native of number of harmonics above threshold.

the pDCR peak is no longer taken into account for image reconstruction. In the following, SM SNRs with thresholds of 0.3, 2.5, and 4.0. as well as the corresponding results of the image reconstruction are shown. A brief review: The spatial distribution of SPIONs to be imaged is a delta sample in the center of a FOV with a size of 15 mm. This distribution (called "sample" in the following plots) is therefore represented by an array containing 15 elements, all of which except the seventh have the value 0.

(a) SM SNR with threshold



(b) Reconstructed image

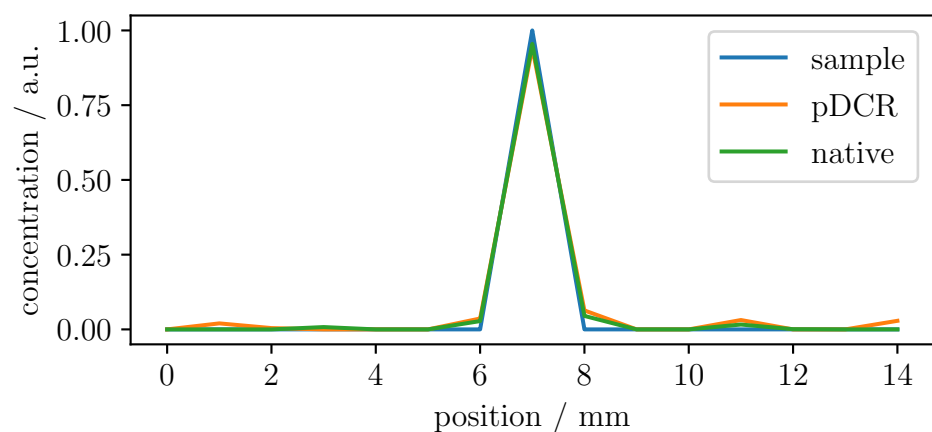
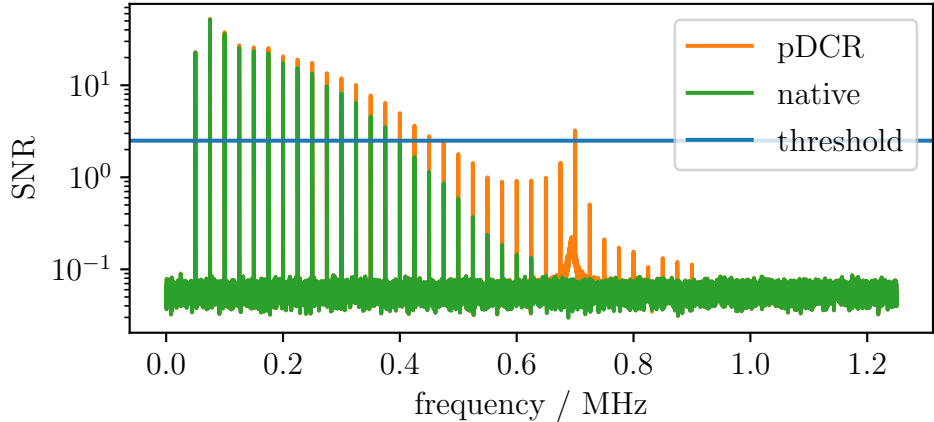


Figure 4.8: SNR threshold at 0.3.

(a) SM SNR with threshold



(b) Reconstructed image

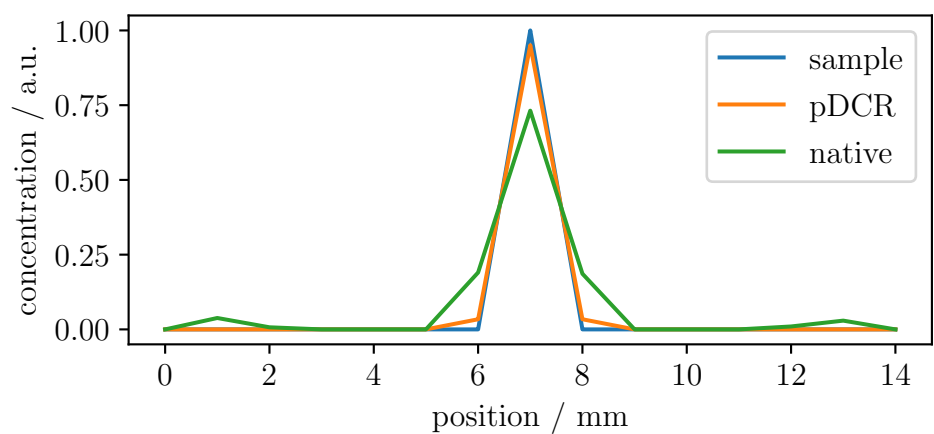


Figure 4.9: SNR threshold at 2.5.

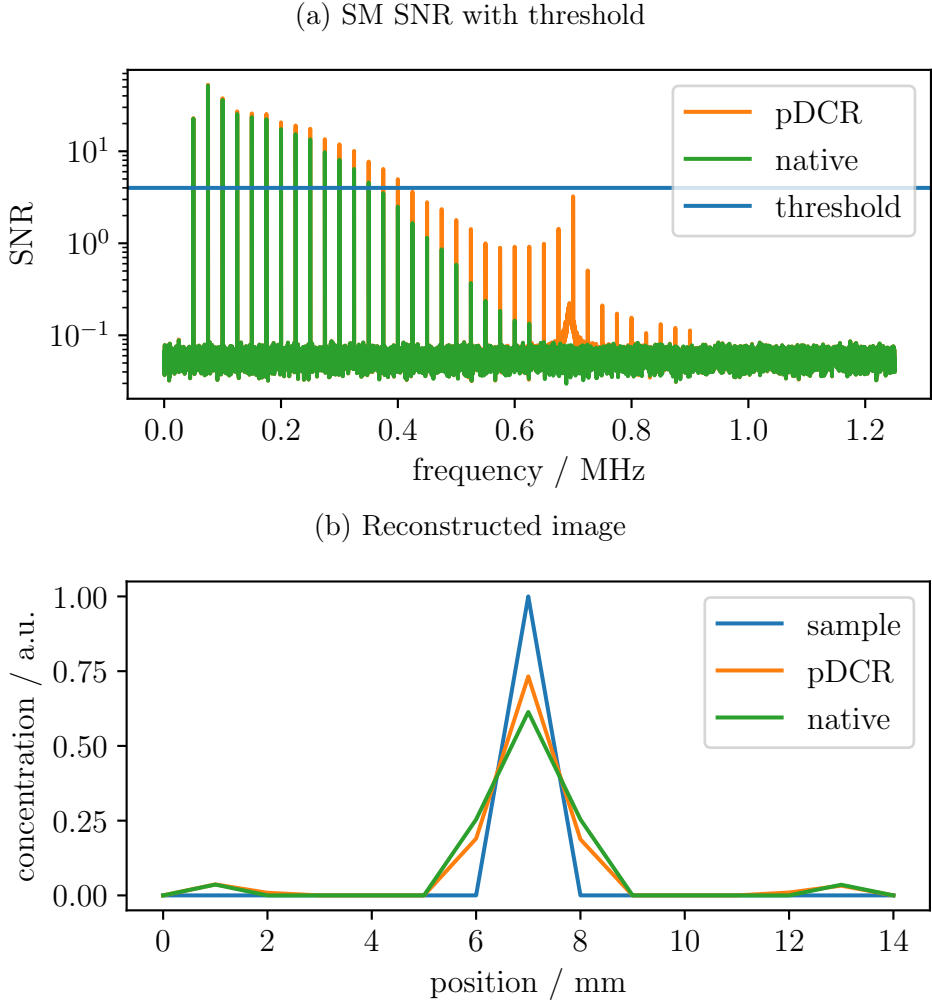


Figure 4.10: SNR threshold at 4.0.

One notes that at the smallest threshold (Fig. 4.8), there is no difference between the reconstruction results with or without the pDCR in use. But as one increases the threshold to 2.5, the advantage of the pDCR comes to light (Fig. 4.9): With the native setup, the amplitude of the peak drops to 75% and also a noticeable decrease in the peaks' full width at half maximum (FWHM) can be seen, while the pDCR image looks as good as before. In the last images shown, the threshold lies above the amplitude of the largest harmonic in the pDCR peak, and thus, no more harmonics of the pDCR peak are used for reconstruction (Fig. 4.10). Only at such a high threshold does the image quality and FWHM of the pDCR setup decrease as well. However, as the difference in the number of harmonics is always greater than 0 (Fig.

4.13), the image quality is still improved with the pDCR in use even for such high thresholds, since amplification by the pDCR already occurs at the first harmonics at low frequencies.

One can not only vary the threshold to directly vary the impact of the pDCR in terms of usable harmonics but also the position of the pDCR peak, i.e. the resonance frequency of the resonant circuit representing the pDCR. The transfer function was manipulated by moving the pDCR peak to the frequencies shown in Tab. 4.2. The manipulated transfer functions can be seen in Fig. 4.11. The resulting SM SNR with the shifted pDCR peaks can be seen in Fig. 4.12.

	pDCR peak frequency [MHz]
no shift	0.694
shift 1	0.725
shift 2	0.754
shift 3	0.786
shift 4	0.816
shift 5	0.935
shift 6	1.057

Table 4.2: Frequencies the pDCR peak is shifted to.

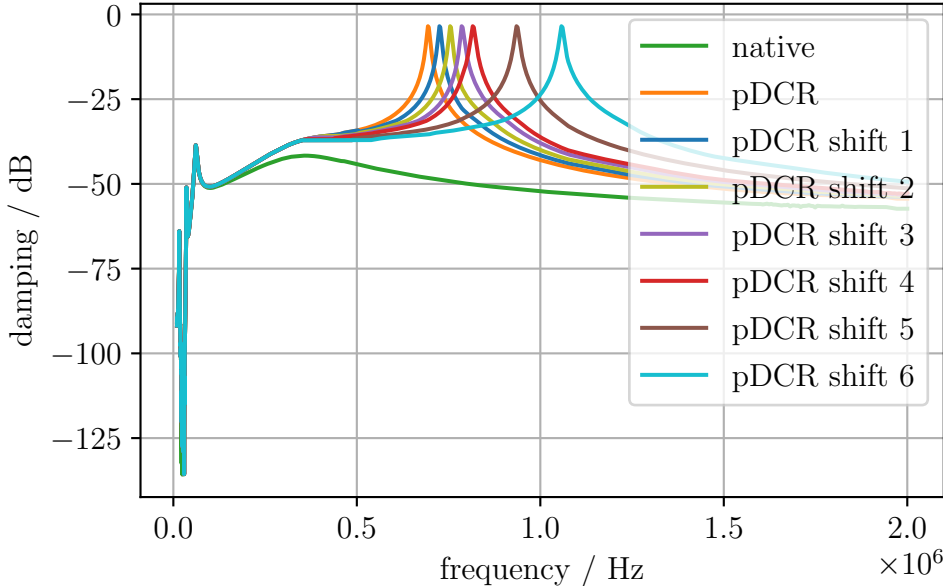


Figure 4.11: Transfer function with different pDCR peak frequency shifts.

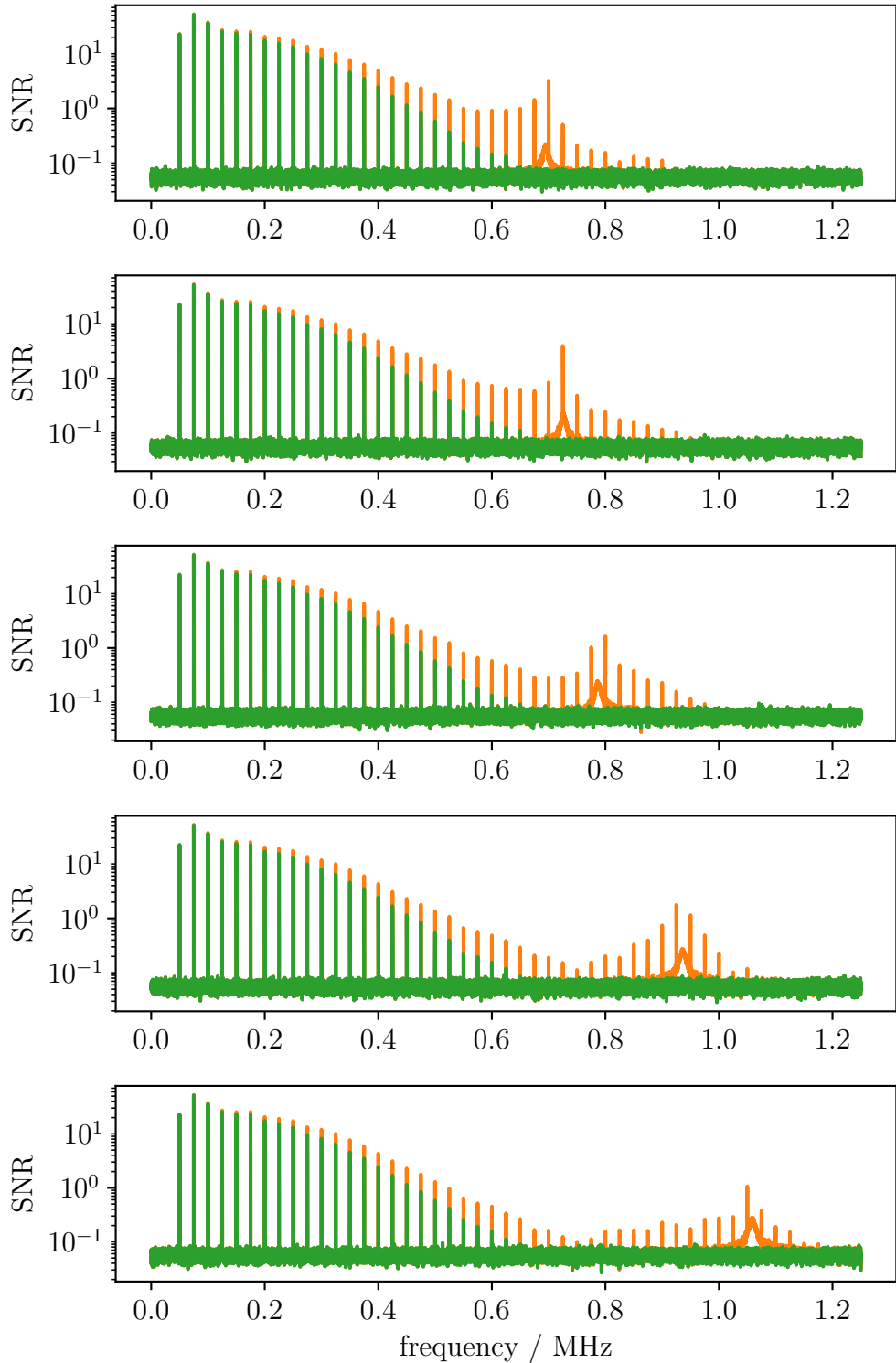


Figure 4.12: The SNR of the SM for the original pDCR peak position and for the shifts 1, 3, 5, and 6 (arranged from top to bottom).

The ratios of number of harmonics that lie above all possible SNR thresholds between 0.1 and 8.0 for all pDCR peak positions, are compared (Fig. 4.13).

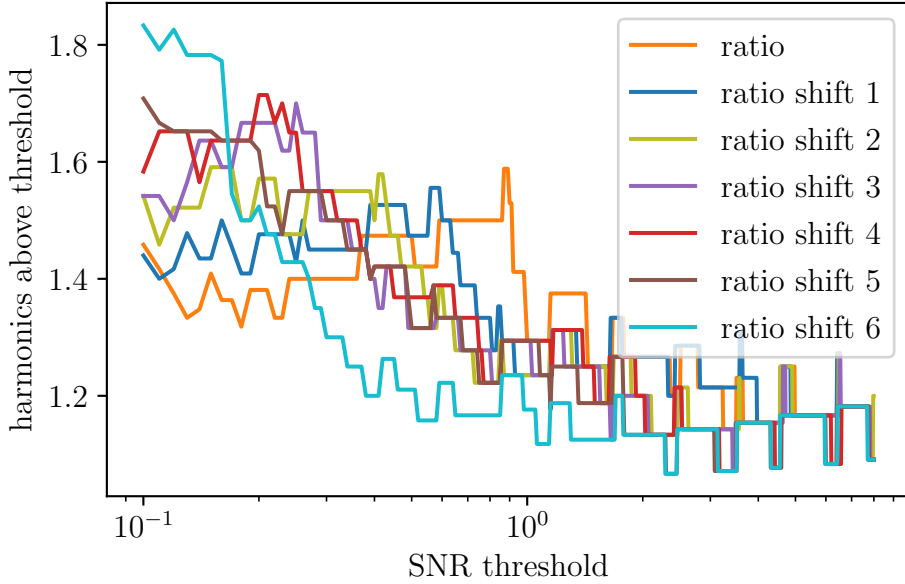


Figure 4.13: Ratio of pDCR and native of number of harmonics above threshold.

## Discussion

The results of the simulations in 1D confirm the expectations. The pDCR fulfills its promises and enhances the SNR, especially at higher harmonics (Fig. 4.5). Therefore, for all tested thresholds, more harmonics are detectable (Fig. 4.13). An improvement in spatial resolution, as well as sensitivity, can be observed especially for higher thresholds, the FWHM in the reconstructions performed with the pDCR is improved (Fig. 4.9).

Tuning the pDCR to higher frequencies seems to have quite an impact (Fig. 4.13). For small thresholds just above the noise level, the higher the frequency of the pDCR peak, the higher the ratio of harmonics that are detectable. If the threshold is chosen higher and higher, this advantage disappears and even turns into the opposite. This can be seen particularly well for pDCR peak shift 6 with a very high frequency of 1.057 MHz: For small thresholds, no pDCR peak position has a greater ratio. From a threshold of 0.3 however, no pDCR peak position has a smaller ratio. For very high

thresholds the differences between the different pDCR peak positions becomes insignificant. It can also be seen that the threshold at which the ratio is greatest moves to smaller thresholds for pDCR peaks at higher frequencies. Peak shift 6 has its maximum already at the start threshold. Furthermore, the maximum ratio increases for pDCR peaks at higher frequencies.

#### 4.1.2 Signal Simulations in 3D

After the influence of the pDCR on the magnetization response to a 1D DF has been investigated in simulation in detail, the same will now be done with a simulation of a 3D DF. Again, the simulation builds upon the program written by Holle but this time a simplified version, which is capable of simulating all 3 dimensions, is used [21]. The course of the simulation does not change noticeably compared to the 1D simulations, which is why the following explanations will be less detailed. It is important to note that in the following only the simulated signal of the  $x$ -channel of the MPI scanner is used because due to its design the pDCR only has an impact on this channel. In reality of course the signals from all channels are used. The signal of the magnetization response in 3D is simulated with the specifications that can be found in Tab. 4.3.

DF frequency x [kHz]	2500/102
DF frequency y [kHz]	2500/196
DF frequency z [kHz]	2500/99
DF amplitude [mT]	14
SF gradient x [T/m]	5
saturation field strength [ $\text{mT}/\mu_0$ ]	1.6
Reconstruction parameters	
number of iterations	30
regularization	5e-5
SM parameters	
number of positions	$5 \times 5 \times 1$
FOV [mm <sup>3</sup> ]	$5 \times 5 \times 1$

Table 4.3: Signal simulation specifications in 3D.

In the simulation of the magnetization response to a 3D DF, a grid of  $5 \times 5 \times 1$  voxels within a 2D FOV of  $5 \times 5 \times 1$  mm<sup>3</sup> within is chosen, yielding an isotropic voxel size of 1 m<sup>3</sup>. A delta sample is again placed in the center voxel of the FOV.

The resulting magnetization spectrum and signal as well as the induced voltage signal and spectrum can be seen in Fig. 4.14. Since the simulation procedure was chosen analogous to the 1D simulation, please refer to section 4.1.1 for more details on the simulation steps, which yield this data.

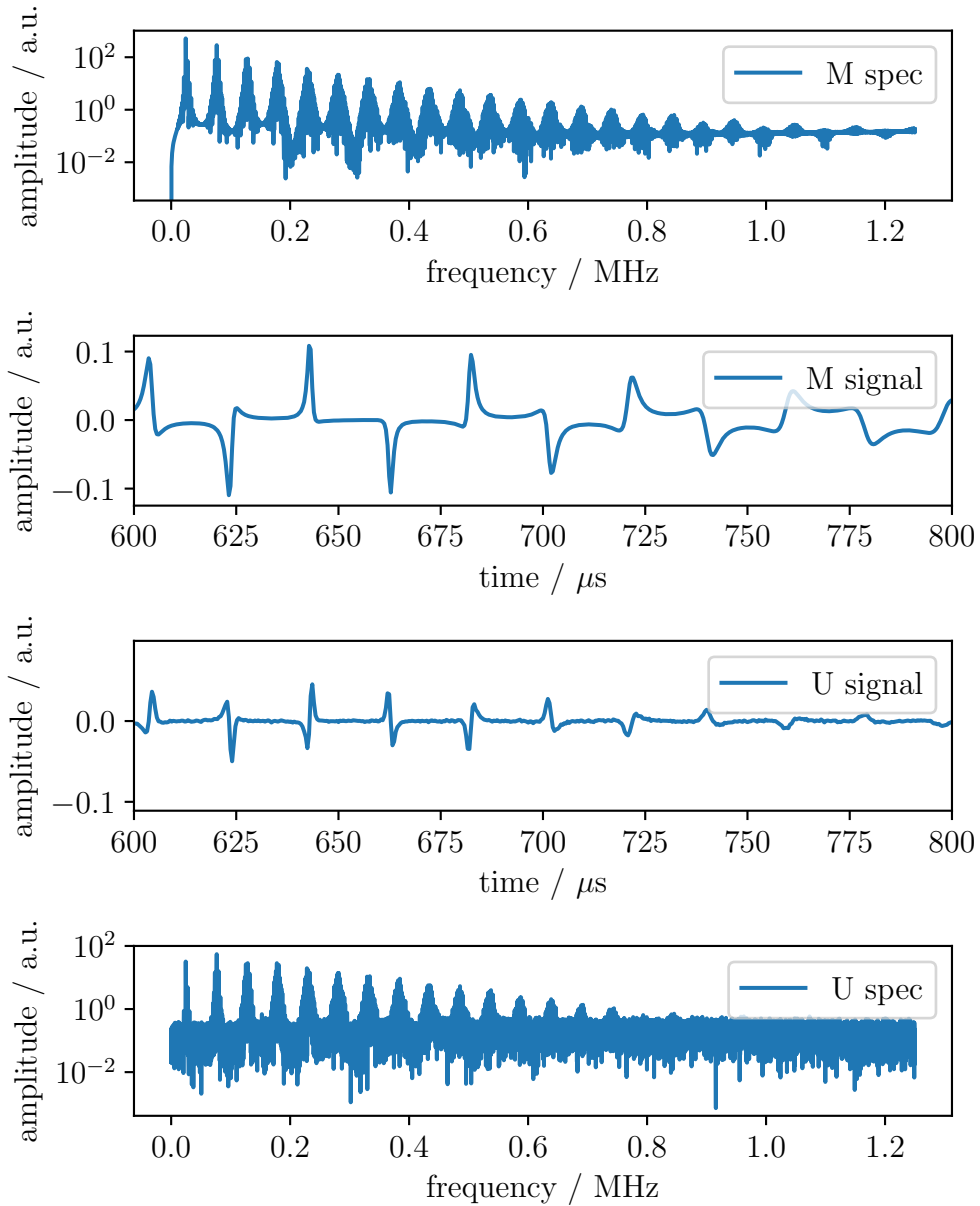


Figure 4.14: Simulation results of the magnetization response to a 3D DF.

## Signal Tuning

The signal tuning procedure is similar to the 1D simulation as well, which is why one can refer to section 4.1.1 for further details. The tuned voltage spectrum averaged over 300 spectra can be seen in Fig. 4.15. The impact of the pDCR is recognizable, closer investigation follows in the next section.

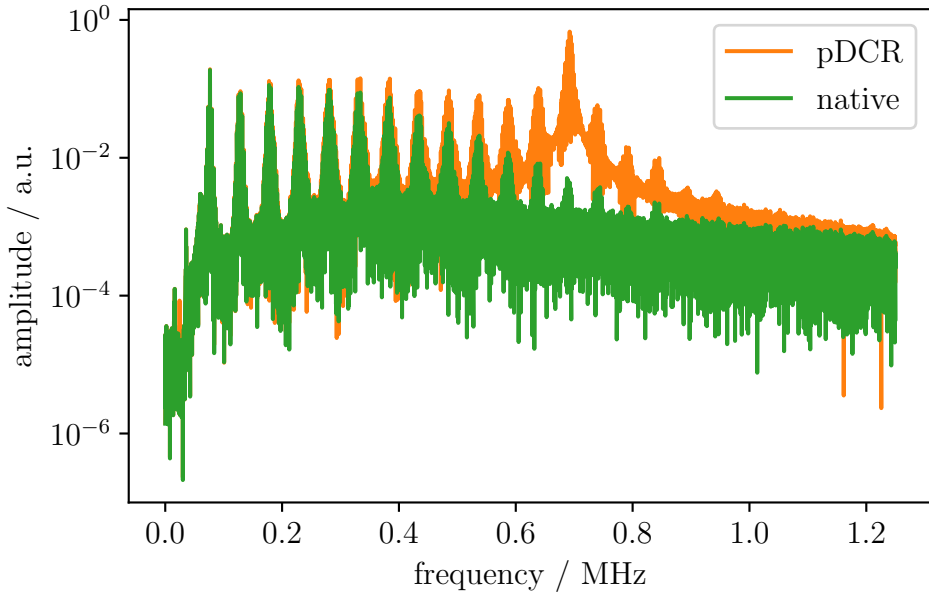


Figure 4.15: 3D simulation signal chain output: magnetization spectrum tuned with the transfer function (mean of 300 simulated spectra).

## Frequency Mixing

With a 1D DF, the identification of the harmonics is simple, as their frequencies are simply multiples of the DF frequency. In 3D, the DF has different frequencies for different directions (Tab. 4.3). Frequency mixing is now occurring: The frequencies of all possible harmonics can be calculated via

$$f_h = m_x f_x + m_y f_y + m_z f_z \quad (4.3)$$

with the mixing factors  $m_i$  and the DF frequencies  $f_i$ . To identify all harmonics in the 3D frequency spectrum, all possible combinations of mixing factors, that result in a mixing frequency inside the frequency range of the spectrum, are calculated.

## SNR and Image Reconstruction

The SNR of the tuned voltage signal spectrum calculated with 300 repetitions can be observed in Fig. 4.16.

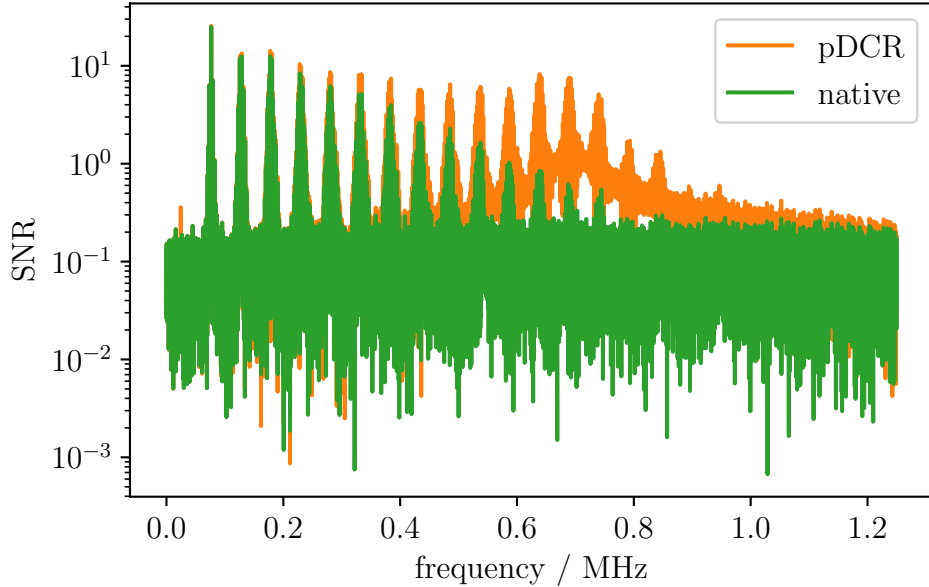


Figure 4.16: SNR in 3D with 300 repetitions.

Just as in the 1D simulation, the gain in SNR at higher harmonics caused by the pDCR is visible. The harmonics are disappearing in the noise floor before 0.8 MHz without the pDCR, while they can still be seen up to approx. 0.9 MHz, when the pDCR is used. Compared to the real measurements that will follow it can be pointed out that the pDCR peak is disproportionately large. This inaccuracy will be, among others, discussed later in more detail.

As in the 1D simulation, the SNR of the SM is chosen to define a threshold for the image reconstruction. This SM SNR is again calculated by taking the SNR for every position of the SM and then taking the mean of the absolutes of these SNRs. The resulting SM SNR can be seen in Fig. 4.17 and will be used for defining thresholds for the image reconstruction from now on.

All possible thresholds between 0.15 and 8.0 are implemented and the number of harmonics, that lie above this threshold, is plotted for the native and the pDCR setup. Furthermore, the difference in the number of harmonics is plotted (Fig. 4.18). The ratio of pDCR to native can be observed in Fig. 4.19.

The course of the data is similar to the 1D simulation. At small thresholds, the difference between the native and the pDCR setup is very large

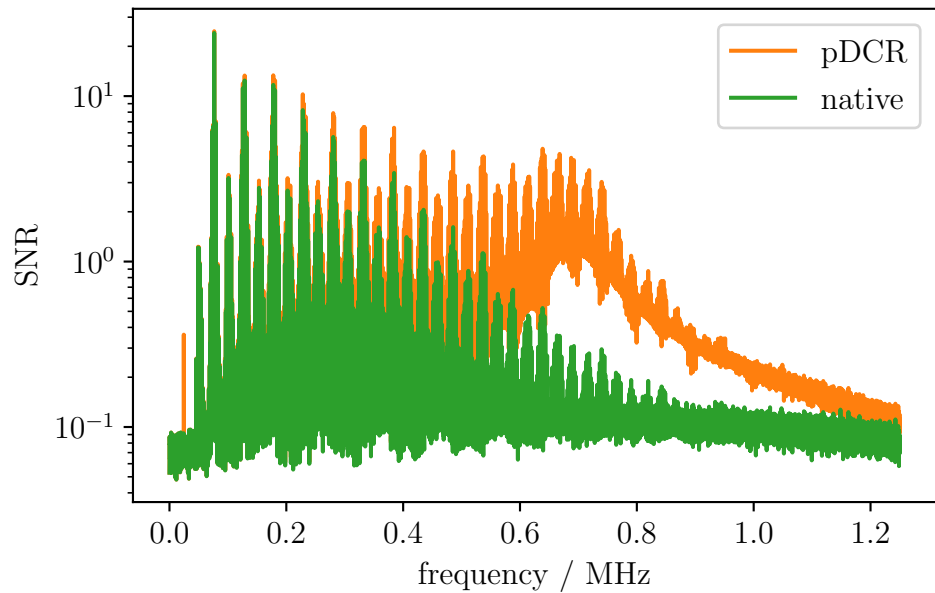


Figure 4.17: SM SNR in 3D with 300 repetitions.

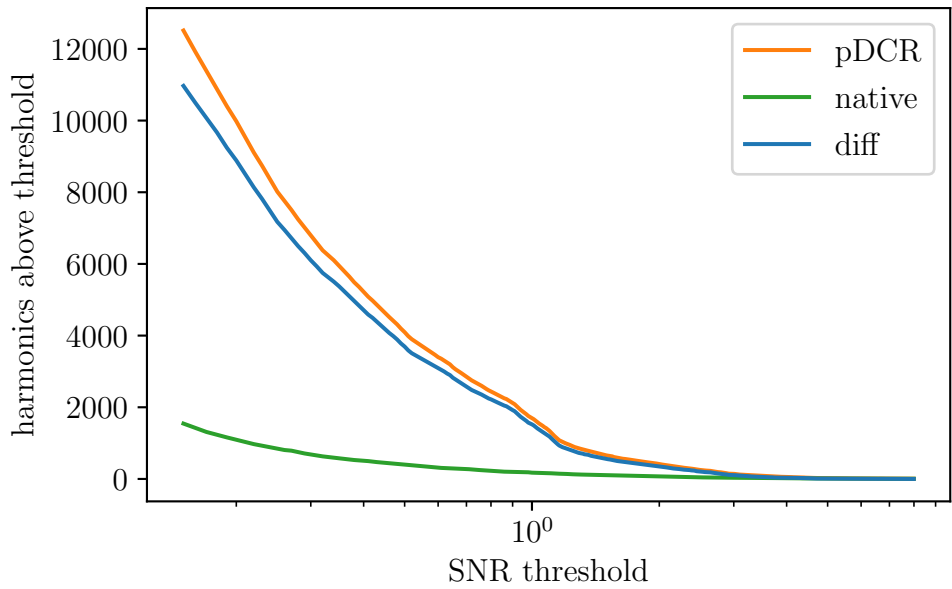


Figure 4.18: Number and difference between pDCR and native of harmonics above the threshold in 3D,  $x$ -axis on logarithmic scale.

but then decreases quite quickly for higher thresholds. The ratio peaks at a threshold of 0.9.

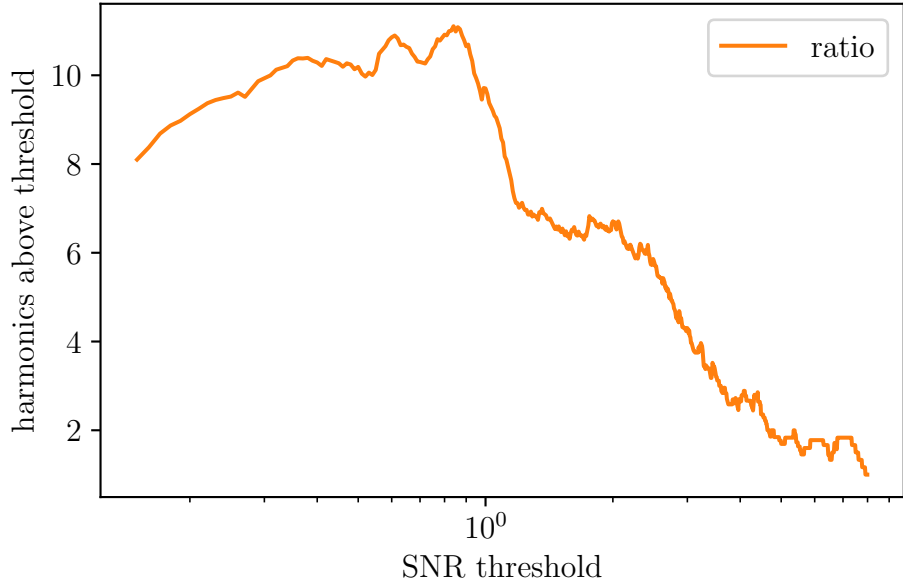


Figure 4.19: Ratio of pDCR to native in terms of harmonics above the threshold in 3D.

To analyze the gain in image quality, one reconstruction is carried out with a threshold of 0.5 and shown in Fig. 4.20.

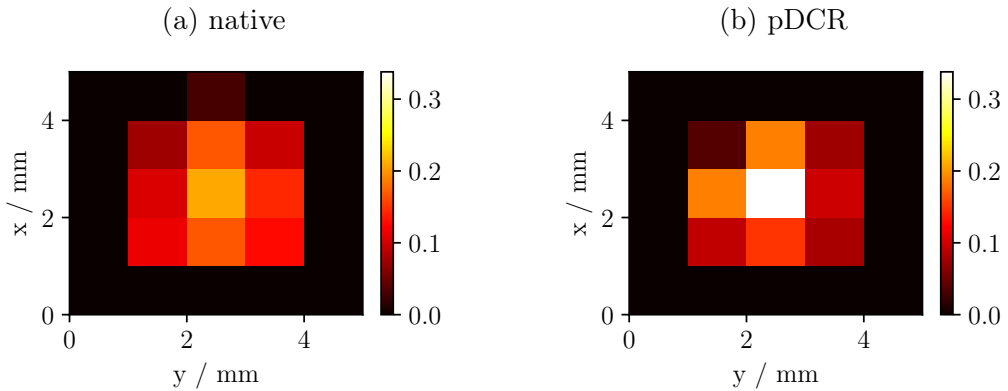


Figure 4.20: Voxel intensity of reconstructed image in 3D with a threshold of 0.5.

Furthermore, the pDCR peak is again shifted to higher frequencies (Tab. 4.2 and Fig. 4.11) and the number of harmonics that lie above the SM SNR threshold are compared for the native and the pDCR setup (Fig. 4.21).

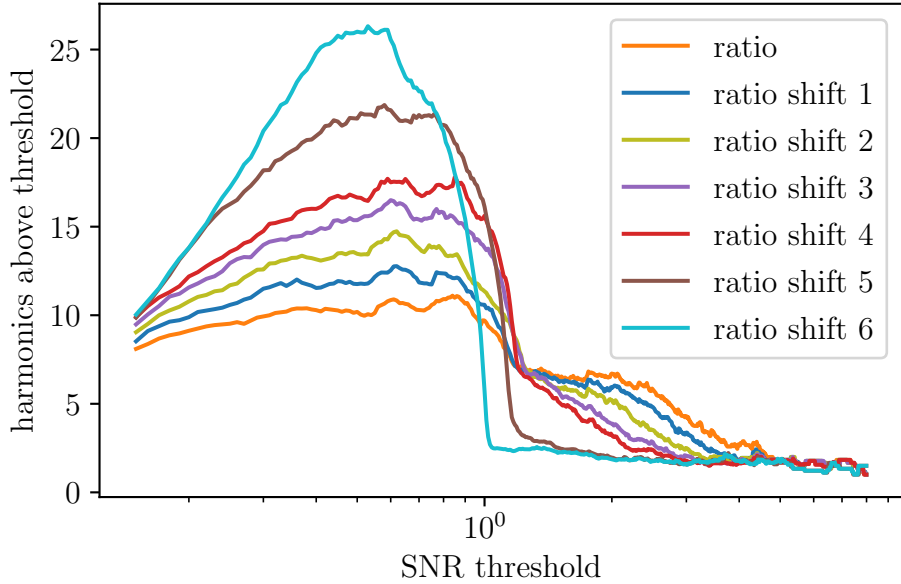


Figure 4.21: Number of harmonics in 3D.

## Discussion

The results from the 1D simulation could be confirmed in 3D. However, the results from the 3D simulation should be taken with a bit more caution. The pattern of the spectrum simulated in 3D does quite differ from the spectrum one would observe in real measurements (see next section). The noise floor baseline is strongly influenced by the pDCR. This is not observable in the measurements. Also, only the  $x$ -channel is used for simulation and reconstruction, while in reality of course all three channels come into use. Nevertheless, the benefits of the pDCR can again be vividly seen: Due to the improved inductive coupling at high frequencies, the harmonics at these frequencies are highly amplified (Fig. 4.16). The highest harmonics can thus, in contrast to the native spectrum, be separated from the noise floor. Therefore, more harmonics can be used for the image reconstruction, which is reflected in an improvement in image quality, especially in terms of spatial resolution and sensitivity (Fig. 4.20). The intensity at the voxels around the center voxel the delta sample was placed at is higher with the native setup, this means more image noise. Moreover, the desired intensity at the center voxel is increased by the pDCR.

Furthermore, the findings of the peak shifting can be concretized in 3D: At small thresholds, again the pDCR peak with the largest frequency provides for the greatest ratio (Fig. 4.21). This holds until a threshold of approx. 1

and then turns into the exact opposite: From this threshold on, this peak position results in the smallest ratio. The maximum of the ratio rises while the threshold it can be found at becomes smaller for peak shifts to greater frequencies.

The position of the pDCR peaks seems to have quite an impact on the effectiveness of the pDCR. However, as the discrete appearance of the spectrum especially concerning the noise has a major influence on this, valid results, from which one could derive handling instructions for optimal construction of the pDCR, should be better obtained via quantitative measurements with the MPI Scanner.

Based on the 3D simulation, all 3 channels could be used for image reconstruction in the future. Finally, the noise floor pattern at the pDCR peaks could be optimized.

## 4.2 Measurements

In the following, the influence of the pDCR on real measurements is investigated. Changes in the SNR are examined and the results of the image reconstruction of a resolution phantom measurement are analyzed in detail.

### 4.2.1 Scanner

All measurements were performed with the Bruker Preclinical Magnetic Particle Imaging instrument, a commercial research system, in combination with Bruker's ParaVision Software. The following settings were selected in ParaVision for system matrix and phantom measurements:

DF frequency $x$ [kHz]	24.5098
DF frequency $y$ [kHz]	26.0417
DF frequency $z$ [kHz]	25.2525
DF amplitude [mT]	14
SF gradient [T/m]	2.5
receivebandwidth [MHz]	1.25

Table 4.4: Scanner properties and settings for measurements carried out with the Bruker Preclinical MPI instrument.

### 4.2.2 Tracer

To ensure that the results are not tracer dependent and to rule out possible other unknown correlations that could lead to a random advantage from using the pDCR, all measurements were performed with two different tracers. One is the C2 tracer, which was developed at the ExMI [24], the other is the commercially available perimag® 102-00-132 (micromod Partikeltechnologie GmbH, Rostock, Germany). The specifications of these tracers can be found in Tab. 4.5.

tracer	C2	perimag® 102-00-132
hydrodynamic diameter [nm]	49.4	130
saturation magnetization [kA/m]	414	> 800

Table 4.5: Specifications of the used tracers, taken from [24] and [25].

### 4.2.3 Phantoms

To record the system matrix and calculate the SNR a delta sample with a volume of  $8 \mu\text{l}$  is used. The gain in image quality is observed with a resolution phantom that has V-shape. Its dimensions can be found in Fig. 4.22.

MPI Resolution phantom  
Material: Acrylic glass (unpolished)  
All dimensions in mm

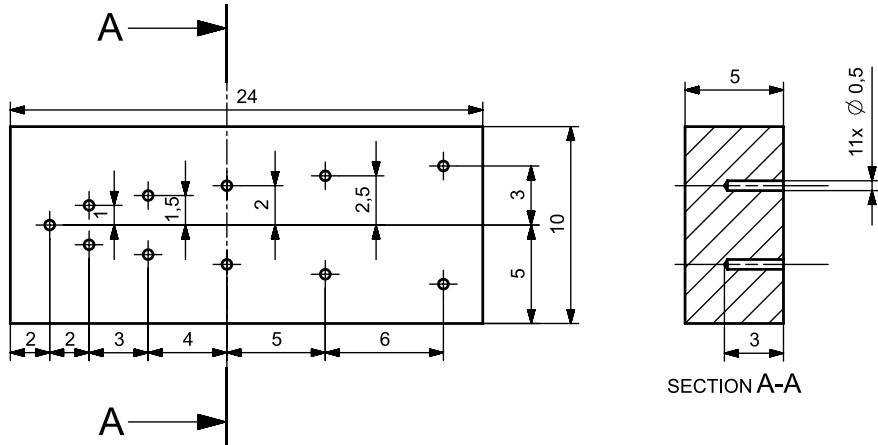


Figure 4.22: Dimensions of the used V-phantom.

#### 4.2.4 Results and Discussion

##### SNR

To observe the gain at higher harmonics, the SNR of the spectra recorded with the mentioned delta sample positioned in the center of the FOV is calculated. The spectrum of the sample as well as the background was recorded with 1000 repetitions. The resulting SNRs for the different tracers can be seen in Fig. 4.23. It should be noted that only the data of the  $x$ -channel is plotted, as the pDCR has a major impact on this channel. All 3 channels were used for the image reconstruction.

In Fig. 4.23, one can identify the influence of the pDCR on the SNR directly: While the harmonics are disappearing in the noise at approx. 0.6 MHz with the use of the native setup, they are visible almost up to 0.8 MHz with the pDCR setup. All harmonics from the beginning on are at least slightly amplified by the pDCR, and from 0.5 MHz on its influence becomes very prominent. From here on, the harmonics are strongly amplified by the pDCR, from 0.63 MHz on the intensities of the harmonics (which normally drop for higher frequencies) are even increasing again until a peak is reached at approx. 0.7 MHz. This progression and the position of the peak was expected based on the measured transfer function. (compare with Fig. 4.2).

##### Image Reconstruction with ParaVision

The image reconstruction procedures for the different tracers in use differ a bit. The measurements with the tracer C2 are carried out with a system matrix FOV of  $25 \times 20 \times 12 \text{ mm}^3$  consisting of  $25 \times 20 \times 8$  voxels, resulting in a voxel size of  $1 \times 1 \times 1.5 \text{ mm}^3$ ; while with perimag<sup>®</sup>, a FOV of  $25 \times 20 \times 13 \text{ mm}^3$  and an isotropic voxel size of  $1 \text{ mm}^3$  is chosen. By choosing at least 13 voxels in height, the denoising of the system matrix is enabled by the ParaVision software, which allows to actively reduce the image noise during the reconstruction. That is the reason why 500 averages were taken for the acquisition of the SM with C2 and only 300 averages with perimag<sup>®</sup> in use. With the denoising enabled fewer averages are needed, as they serve the same purpose. This allows more voxels to be imaged while keeping the scanning time within practical limits. In both cases, one chooses to determine the background after every 25th measurement for the acquisition of the SM, resulting in scan times of 14 resp. 14.5 h. For the image reconstruction, a number of 30 iterations and a regularization parameter of 5e-5 for C2 and 1e-4 for perimag<sup>®</sup> is chosen. In both cases, an SNR threshold of 3.0 and a maximum mixing order of 25 is chosen. As already mentioned, in the case of the perimag<sup>®</sup> tracer, one is also able to activate the SM denoising, whereby

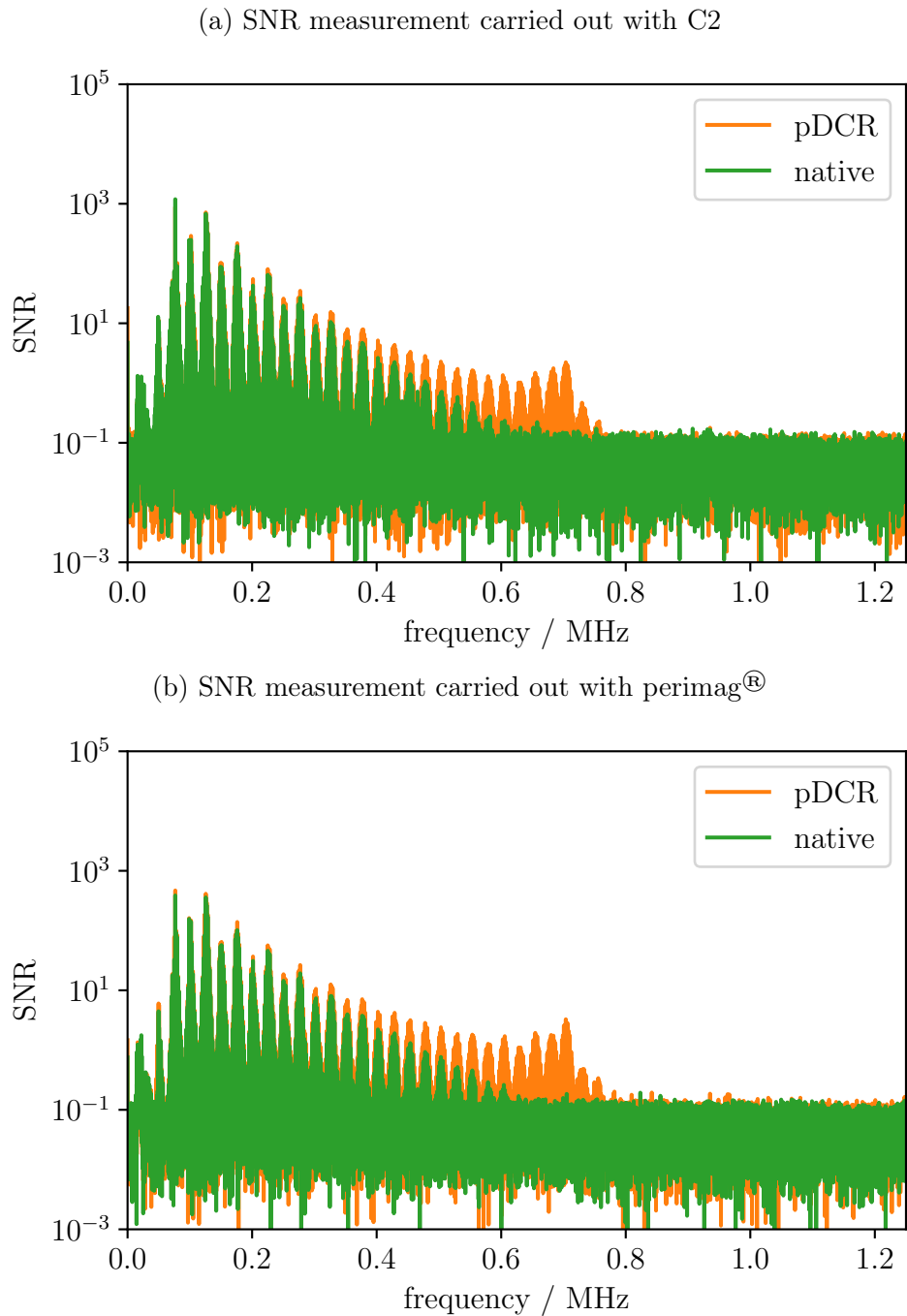


Figure 4.23: SNR measurements carried out with 1000 repetitions.

one has chosen the threshold operator "hard", transformation type "Fourier" and a weighting factor of 5. Background measurements for correction were

taken in any case. The system matrix for the two different tracers is recorded once with and once without the pDCR. The measurement of the V-phantom is also performed once with and once without this device. The image reconstructions are then performed with the respective system matrices and the parameters mentioned above. The results are shown in the following.

It should be noted: The V-phantom is inserted into the scanner in such an orientation, that the V-letter can be recognized in the  $x$ - $y$ -plane. Thus, one of the planes in the reconstructed image will contain most of the tracer and therefore will show highest intensity. In the following images, the top row shows this prominent plane in which the phantom was mainly located, while the mean of all planes is shown below. On the left, the image taken without and on the right the image taken with the pDCR is shown.

Unfortunately, the MPI scanner resp. the ParaVision Software normalizes the signal for each measurement, so a comparison of the absolute intensities between native and pDCR setup was not possible. Although the MPI measurement is inherently quantitative, this quality is nullified by normalization. First, the reconstructed images from the ParaVision software are discussed here, before an alternative reconstruction method is applied in the next section, which allows a comparative analysis of the absolute intensities. The impact of the pDCR becomes impressively apparent in the reconstructed images of the measurements performed with the C2 tracer (Fig. 4.24):

- The individual point samples of the V-phantom appear in total way less blurred in the reconstructed image with the pDCR (this is especially very well visible from about  $x=12.5$  mm to the top).
- In the area where the dots come closer to each other and the smearing without pDCR leads to the fact that individual dots are no longer recognizable as such, the advantage of using the pDCR becomes particularly visible. While from approx.  $x=17.5$  mm (i.e. from the third level in the V-phantom, where the dots' centers have a distance of 3 mm) without the pDCR single dots are hard to be recognized in the image, with pDCR, one can recognize two dots separated from each other. However, in the first two planes of the phantom (center distance 2 mm and single point), individual dots are no longer recognizable with the pDCR as well.

Also in the measurements carried out with the commercial perimag<sup>®</sup> tracer, the impact of the pDCR becomes visible (Fig. 4.25):

- As seen in the measurements with C2, the spatial resolution is increased, the dots are more pronounced when using the pDCR (here

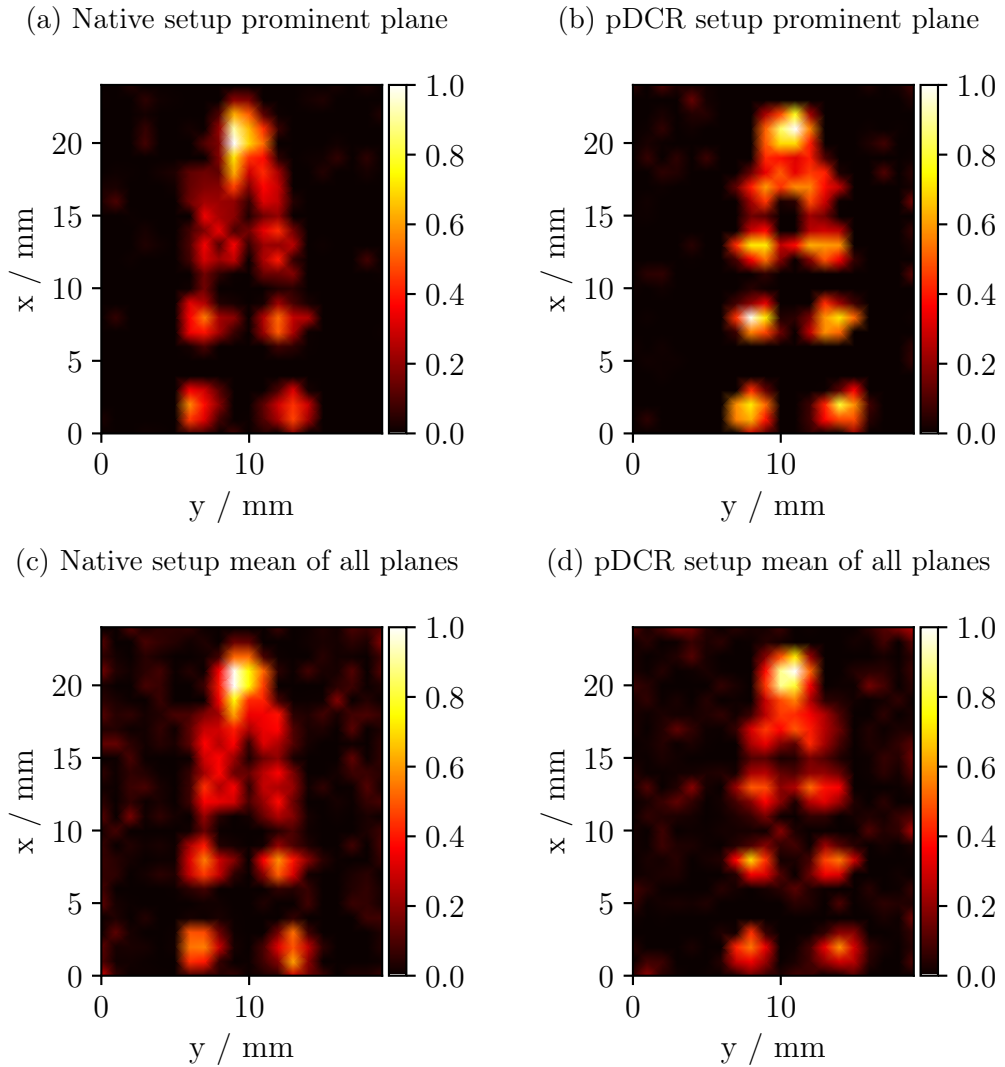


Figure 4.24: Reconstructed images with the C2 tracer with the ParaVision software.

strongly visible in the fourth plane of the phantom at about  $x=13$  mm).

- The merging of dots from  $x=17.5$  mm (i.e. from a horizontal distance between two dots of 3 mm) is also more pronounced without pDCR and thus, makes it more difficult to identify individual dots as such.

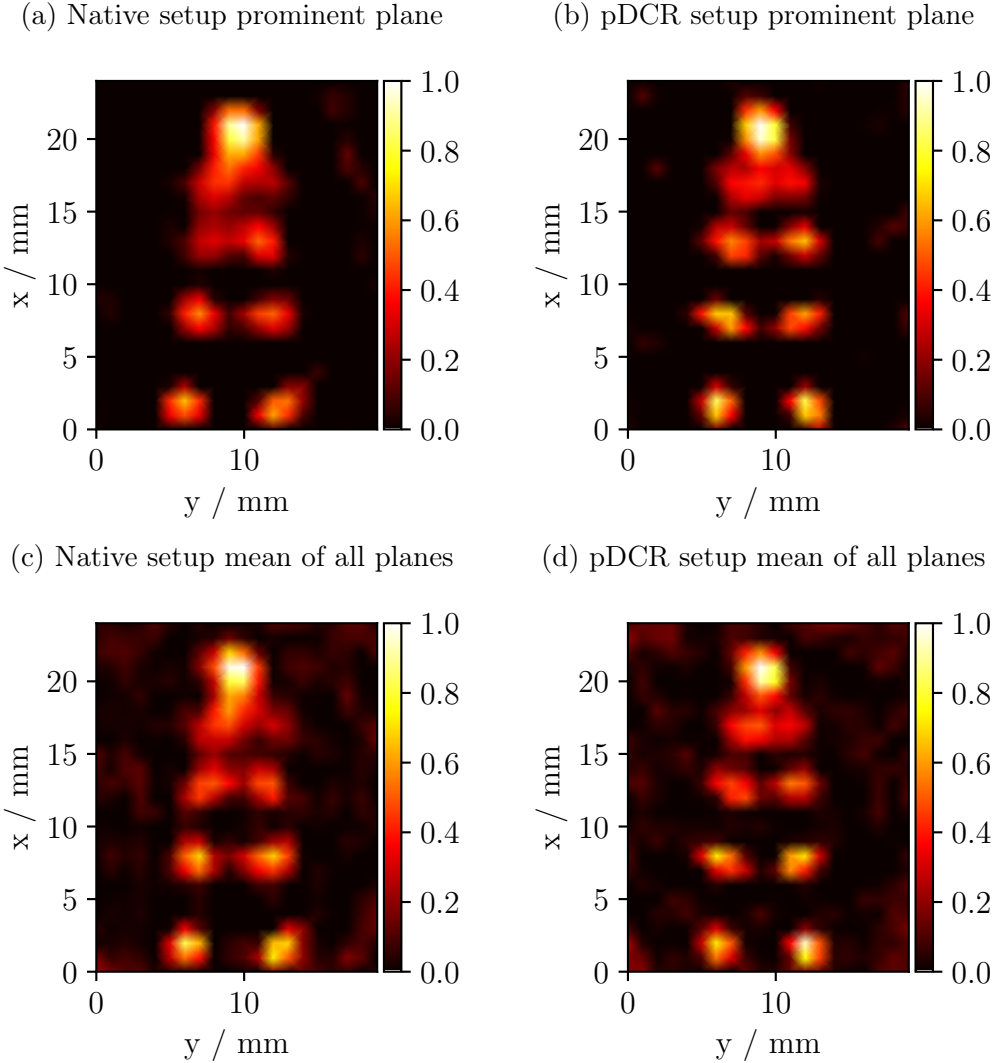


Figure 4.25: Reconstructed images with the perimag® tracer carried out with the ParaVision software.

### Image Reconstruction with Python

To avoid the normalization in the image reconstruction and thus, the loss of important information for the analysis of the influence of the pDCR, a Python program was developed by Franziska Schrank [26]. This is an alternative to the reconstruction with the ParaVision software and reconstructs images with absolute and not normalized intensities.

For all reconstructions with the mentioned python program, the SM SNR was chosen to be 3, the regularization is set to 5e-5 and 500 iterations are

performed. The SM denoising is activated with a denoising threshold of 0.01 for the C2 and 0.02 for the perimag® measurements. The threshold operator "soft" and transformation type "Discrete Cosine Transformation (DCT)" is chosen.

The following two figures are representing the same measurement results as the previous two. What is different is that the reconstructed intensities are now absolute and can be compared between the different plots. It should be noted, however, that for the plots representing the prominent plane, other maximum values for the color bar have been chosen, since the very low mean values would otherwise hardly be distinguishable from the background.

- In the reconstructed images with the C2 and the perimag® tracer (Fig. 4.26 and 4.27) the increased spatial resolution caused by the pDCR can be observed again. This can be seen well in the prominent plane as well as in the average of all planes.
- Now it is also possible to make statements about the intensities: (a) Without pDCR, a large intensity maximum is registered at the top of the V-phantom, while the lower dots show a rather low intensity. (b) The pDCR increases the intensities of the lower, individual dots.

### Conclusion of V-phantom Measurements

It can be said that the use of the pDCR results in an improvement in image quality. The spatial resolution is increased; individual dots are less blurred. From a certain minimum distance between two dots, individual dots are of course no longer recognizable as such, even using the pDCR, and merge with their neighbors (angular resolution). However, this minimum distance is lowered by the pDCR, the identification of single dots in a dense cluster of dots is better possible.

However, beyond the horizon of this work remains to be investigated. The impact of the the pDCR peak shifting on real measurements and detailed studies on the sensitivity are only two examples.

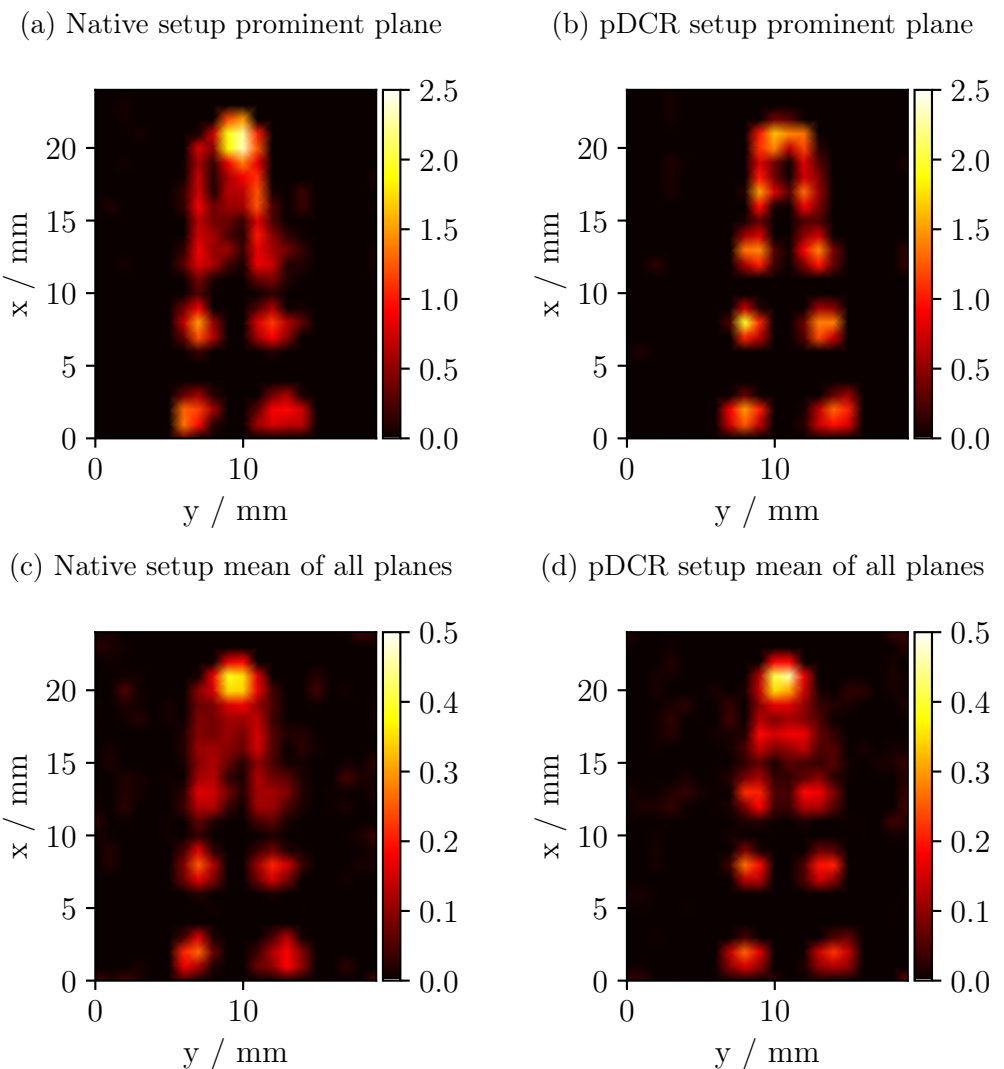


Figure 4.26: Reconstructed images with the C2 tracer carried out with the Python reconstruction program.

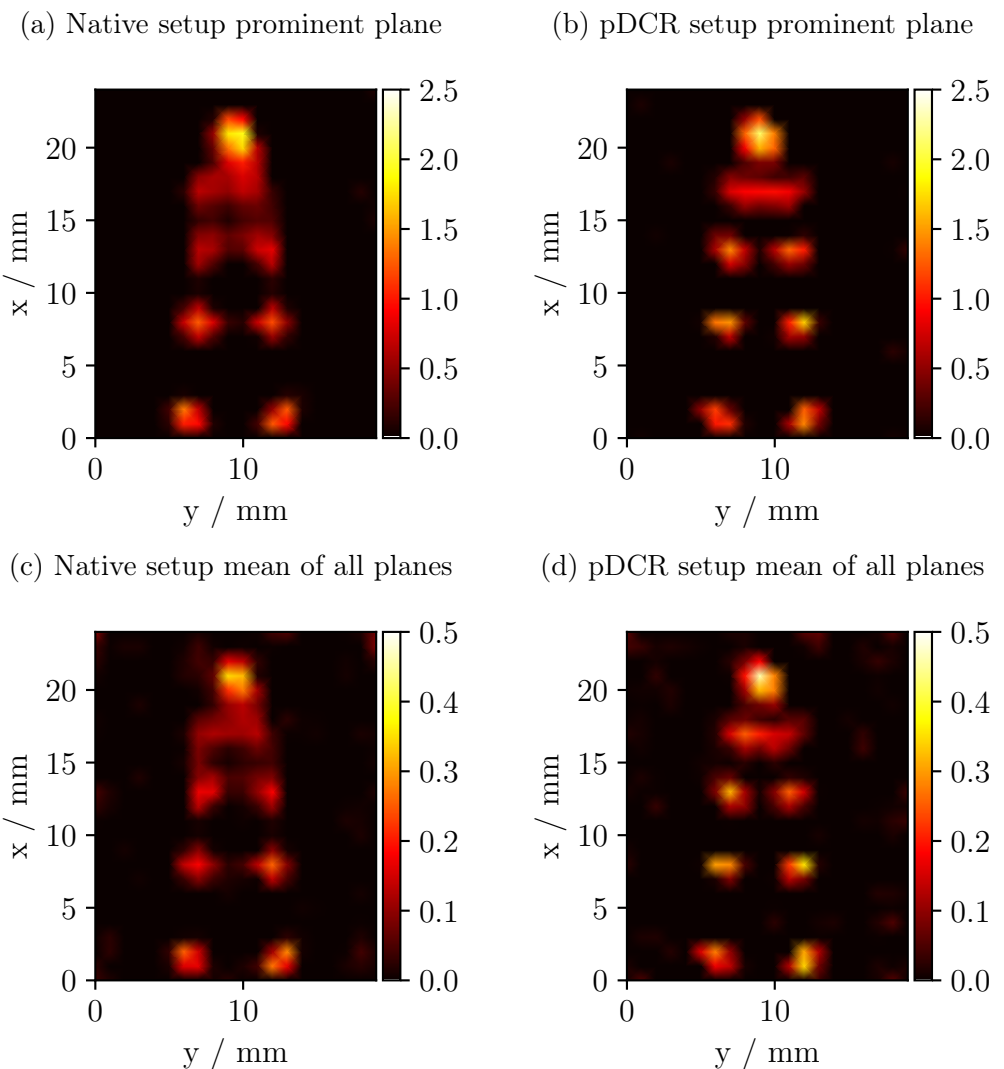


Figure 4.27: Reconstructed images with the perimag® tracer with the Python reconstruction program.

## 5 | Conclusion and Outlook

The goal of this thesis was to further investigate, what the just recently invented pDCR is capable of. Up to now, only a proof of concept was accomplished, which, however, gave rise to hopes of great improvements in image quality in MPI, especially in terms of spatial resolution. The investigation of the pDCR and its effect on the MPI signal chain, the SNR, and the reconstructed images was accomplished via simulations in 1D and 3D as well as measurements carried out with the Bruker Preclinical MPI instrument.

The simulations showed the great impact of the pDCR. It improves the signal of the MPI scanner by amplifying especially the higher harmonics. Not only the SNR of already visible harmonics is amplified, but also further harmonics that were previously not detectable are made apparent. As a result, an improvement in spatial resolution can be seen in the reconstructed images. Also, the impact of shifts of the pDCR peak was analyzed in detail. It resulted: For small thresholds, shifting the pDCR peak to higher frequencies gives an advantage in terms of the number of harmonics that can be used for image reconstruction.

The impact occurring in the simulations could be reproduced by real measurements. The signal amplification, especially the improvement of the SNR at high frequencies could be impressively demonstrated. An advancement in image quality could also be observed as the spatial resolution is clearly improved, meaning that close objects can be better separated.

Moreover, it is particularly impressive what a simple but effective design made these improvements possible. The cost-effective pDCR device is also appealing from an economic point of view.

It is also clear that the potential of pDCR is far from exhausted: As could be seen, the positioning of the pDCR peak seems to have an impact on the performance of the pDCR. Therefore, especially designs with an adjustable resonant frequency seem to be promising. Also, it seems reasonable to design the pDCR so that its effect is not limited to the  $x$ -channel, but benefits all scanner channels. Another promising concept is the use of a miniature pDCR that directly encloses the delta sample used to record the system matrix.

# Closing Remarks

The field of medical imaging remains exciting and always has new surprises in store. The author looks forward to the future of this constantly reinventing field of research and is eager to see what changes will revolutionize it next. Concerning hardware, as one can see, there are no limits to the inventive spirit. The countless research institutes of this world will constantly come up with new and innovative designs that will turn more and more of what is theoretically possible into reality. In terms of software, AI will presumably challenge many of the things we take for granted right now and turn the work routines of radiologists upside down.

Whether in the nineteenth century at the Physics Institute of the University of Würzburg or in the twenty-first century at the Philips Research lab in Hamburg or the ExMI of RWTH Aachen University: German research institutes seem to be a special hotbed for discoveries that make visible what could not be seen before.

# Appendix

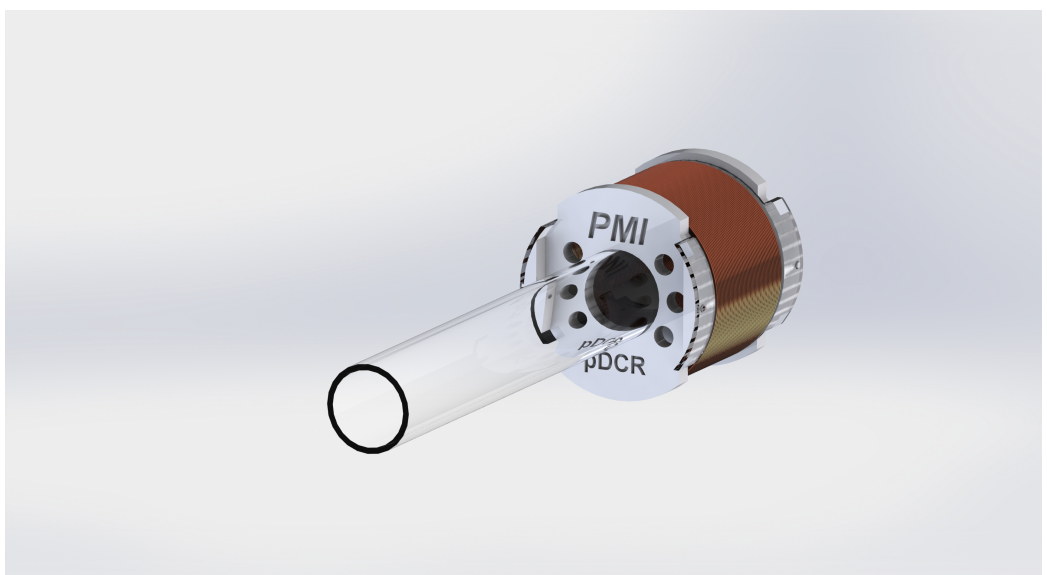


Figure 5.1: Rendered pDCR design

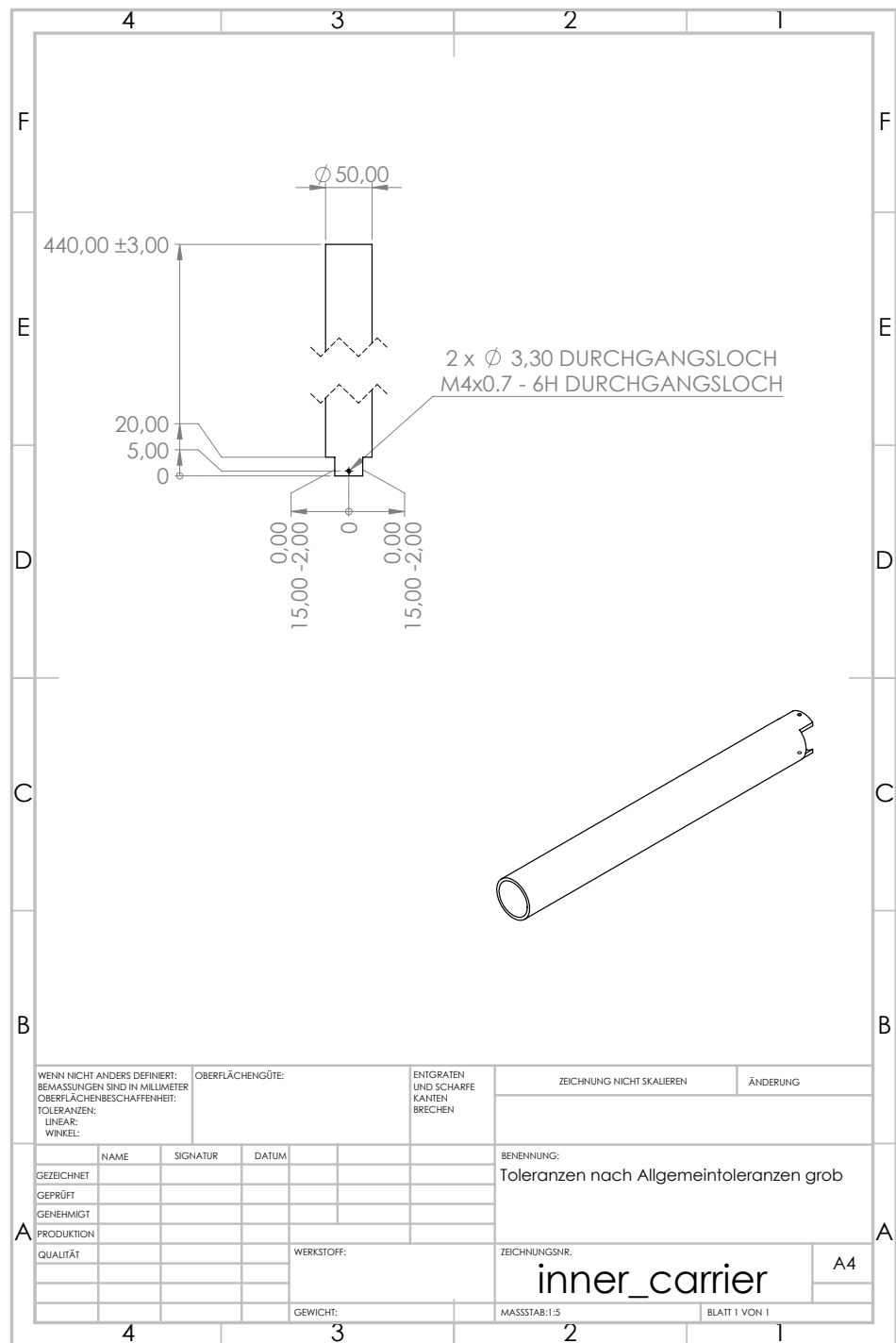


Figure 5.2: pDCR inner carrier

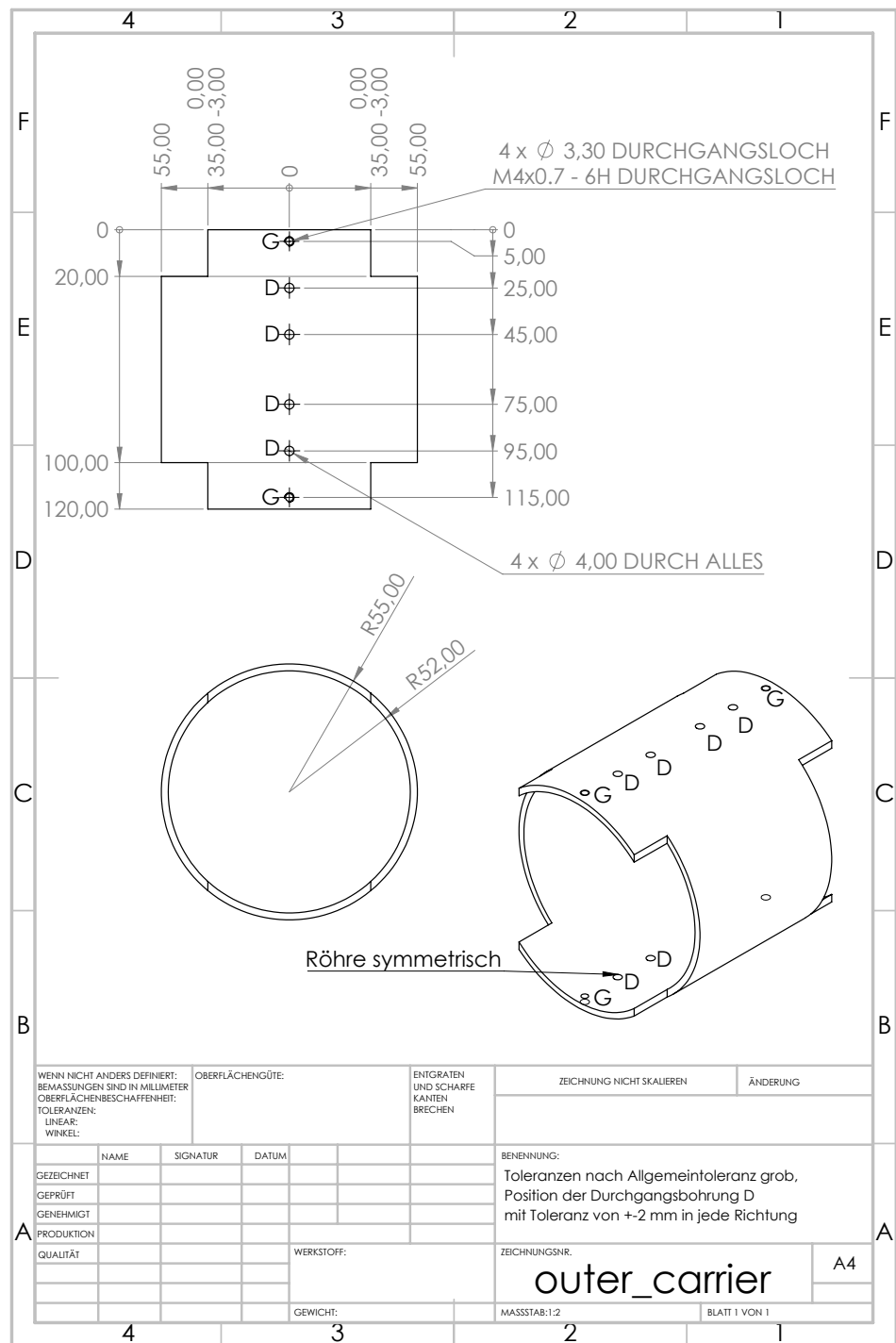


Figure 5.3: pDCR outer carrier

# List of Abbreviations

<b>CT</b>	computed tomography
<b>DF</b>	drive field
<b>FF</b>	focus field
<b>FFP</b>	field-free point
<b>FOV</b>	field of view
<b>MPI</b>	magnetic particle imaging
<b>MRI</b>	magnetic resonance imaging
<b>pDCR</b>	passive dual coil resonator
<b>PET</b>	positron emission tomography
<b>SM</b>	system matrix
<b>SF</b>	selection field
<b>SNR</b>	signal-to-noise ratio
<b>SPION</b>	superparamagnetic iron oxide nanoparticle

# List of Figures

2.1	Schematic drawing of a SPION (taken from [7]). . . . .	4
2.2	Nonlinear magnetization curve: Relation between the external magnetic field $H$ and the magnetization of the particles $M$ (taken from [7]). . . . .	5
2.3	The particles' magnetic moments align along the magnetic field until saturation is reached (taken from [7]). . . . .	5
2.4	Counterclockwise: Particle magnetization (already seen in Fig. 2.2), excitation signal (DF) and resulting magnetization response of the SPIONs (taken from [9]). . . . .	6
2.5	Induced particle signal in time and frequency space (taken from [7]). . . . .	7
2.6	Selection field with field-free point (FFP) (taken from [7]). . .	8
2.7	2D and 3D Lissajous trajectory (taken from [7]). . . . .	8
2.8	MPI scanner setup (taken from [9]). . . . .	10
2.9	MPI Scanner signal chain (taken from [9]). . . . .	11
3.1	Original square wave function and partial sums of the Fourier series for $n=\{5,15,100\}$ elements. . . . .	14
3.2	Schematics of the pDCR functionality (taken from [8]). . . .	15
3.3	Photograph of the assembled pDCR in front of the Bruker MPI bore. . . . .	17
4.1	Simulation results for the magnetization response to a 1D DF. From top to bottom: particles' magnetization response in frequency space, in time space, voltage induced in the receive coils in time space, in frequency space . . . . .	21
4.2	Transfer function for native and pDCR setup, logarithmic scale on $x$ -axis. . . . .	23
4.3	1D simulation signal chain output: magnetization spectrum tuned with the transfer function (mean of 500 simulated spectra). . . . .	24
4.4	SNR in 1D with 500 repetitions. . . . .	25
4.5	SNR of SM in 1D with 500 repetitions. . . . .	26

4.6	Comparison and difference between pDCR and native of number of harmonics above threshold. $x$ -axis on logarithmic scale.	26
4.7	Ratio of pDCR to native of number of harmonics above threshold.	27
4.8	SNR threshold at 0.3.	28
4.9	SNR threshold at 2.5.	29
4.10	SNR threshold at 4.0.	30
4.11	Transfer function with different pDCR peak frequency shifts.	31
4.12	The SNR of the SM for the original pDCR peak position and for the shifts 1, 3, 5, and 6 (arranged from top to bottom).	32
4.13	Ratio of pDCR and native of number of harmonics above threshold.	33
4.14	Simulation results of the magnetization response to a 3D DF.	35
4.15	3D simulation signal chain output: magnetization spectrum tuned with the transfer function (mean of 300 simulated spectra).	36
4.16	SNR in 3D with 300 repetitions.	37
4.17	SM SNR in 3D with 300 repetitions.	38
4.18	Number and difference between pDCR and native of harmonics above the threshold in 3D, $x$ -axis on logarithmic scale.	38
4.19	Ratio of pDCR to native in terms of harmonics above the threshold in 3D.	39
4.20	Voxel intensity of reconstructed image in 3D with a threshold of 0.5.	39
4.21	Number of harmonics in 3D.	40
4.22	Dimensions of the used V-phantom.	42
4.23	SNR measurements carried out with 1000 repetitions.	44
4.24	Reconstructed images with the C2 tracer with the ParaVision software.	46
4.25	Reconstructed images with the perimag® tracer carried out with the ParaVision software.	47
4.26	Reconstructed images with the C2 tracer carried out with the Python reconstruction program.	49
4.27	Reconstructed images with the perimag® tracer with the Python reconstruction program.	50
5.1	Rendered pDCR design	53
5.2	pDCR inner carrier	54
5.3	pDCR outer carrier	55

# List of Tables

1.1	Comparison of the different imaging techniques (taken from [7]).	2
4.1	Signal generation parameters and reconstruction parameters in the 1D simulation. For reconstruction the Kaczmarz algorithm was used.	20
4.2	Frequencies the pDCR peak is shifted to.	31
4.3	Signal simulation specifications in 3D.	34
4.4	Scanner properties and settings for measurements carried out with the Bruker Preclinical MPI instrument.	41
4.5	Specifications of the used tracers, taken from [24] and [25].	42

# Bibliography

- [1] Sui-Lee Wee. “As Deaths Mount, China Tries to Speed Up Coronavirus Testing”. In: *The New York Times. World* (Feb. 9, 2020). ISSN: 0362-4331. URL: <https://www.nytimes.com/2020/02/09/world/asia/china-coronavirus-tests.html> (visited on 11/20/2020).
- [2] SPECTARIS. *Zahlen, Fakten & Publikationen*. URL: <https://www.spectaris.de/photonik/zahlen-fakten-und-publikationen/amp.html> (visited on 01/28/2021).
- [3] S.W. Lee, S.K. Hilal, and Z.H. Cho. “A Multinuclear Magnetic Resonance Imaging Technique-Simultaneous Proton and Sodium Imaging”. In: *Magnetic Resonance Imaging* 4.4 (Jan. 1986), pp. 343–350. ISSN: 0730725X. DOI: 10.1016/0730-725X(86)91044-1. URL: <https://linkinghub.elsevier.com/retrieve/pii/0730725X86910441> (visited on 01/12/2021).
- [4] Katsuyuki Taguchi and Jan S. Iwanczyk. “Vision 20/20: Single Photon Counting x-Ray Detectors in Medical Imaging: Vision 20/20: Photon Counting Detectors”. In: *Medical Physics* 40.10 (Sept. 12, 2013), p. 100901. ISSN: 00942405. DOI: 10.1118/1.4820371. URL: <http://doi.wiley.com/10.1118/1.4820371> (visited on 01/12/2021).
- [5] Bjoern Weissler et al. “A Digital Preclinical PET/MRI Insert and Initial Results”. In: *IEEE TRANSACTIONS ON MEDICAL IMAGING* 34.11 (2015), p. 13.
- [6] Bernhard Gleich and Jürgen Weizenecker. “Tomographic Imaging Using the Nonlinear Response of Magnetic Particles”. In: *Nature* 435.7046 (June 2005), pp. 1214–1217. ISSN: 0028-0836, 1476-4687. DOI: 10.1038/nature03808. URL: <http://www.nature.com/articles/nature03808> (visited on 10/25/2020).
- [7] Tobias Knopp and Thorsten M. Buzug. *Magnetic Particle Imaging: An Introduction to Imaging Principles and Scanner Instrumentation*. Heidelberg: Springer, 2012. 204 pp. ISBN: 978-3-642-04198-3.

- [8] S D Reinartz et al. “Feasibility of a Spatial Resolution Enhancement by a Passive Dual Coil Resonator (pDCR) Insert for Large Bore MPI Systems”. In: (), p. 2.
- [9] T Knopp, N Gdaniec, and M Möddel. “Magnetic Particle Imaging: From Proof of Principle to Preclinical Applications”. In: *Physics in Medicine & Biology* 62.14 (June 23, 2017), R124–R178. ISSN: 1361-6560. DOI: 10.1088/1361-6560/aa6c99. URL: <https://iopscience.iop.org/article/10.1088/1361-6560/aa6c99> (visited on 10/25/2020).
- [10] Subhankar Bedanta and Wolfgang Kleemann. “Supermagnetism”. In: *Journal of Physics D: Applied Physics* 42.1 (Jan. 7, 2009), p. 013001. ISSN: 0022-3727, 1361-6463. DOI: 10.1088/0022-3727/42/1/013001. URL: <https://iopscience.iop.org/article/10.1088/0022-3727/42/1/013001> (visited on 11/24/2020).
- [11] T. Knopp et al. “Model-Based Reconstruction for Magnetic Particle Imaging”. In: *IEEE Transactions on Medical Imaging* 29.1 (Jan. 2010), pp. 12–18. ISSN: 0278-0062, 1558-254X. DOI: 10.1109/TMI.2009.2021612. URL: <http://ieeexplore.ieee.org/document/4912405/> (visited on 01/31/2021).
- [12] S Kaczmarz. “Angenäherte Auflösung Yon Systemen Linearer Gleichungen”. In: *Bull. Intern. Acad. Polonaise Sci. Lettres (Cracovie)* (1937), pp. 355–357.
- [13] Charles R. Harris et al. “Array Programming with NumPy”. In: *Nature* 585.7825 (Sept. 1, 2020), pp. 357–362. ISSN: 1476-4687. DOI: 10.1038/s41586-020-2649-2. URL: <https://doi.org/10.1038/s41586-020-2649-2>.
- [14] Jürgen Rahmer et al. “Signal Encoding in Magnetic Particle Imaging: Properties of the System Function”. In: *BMC Medical Imaging* 9.1 (Dec. 2009), p. 4. ISSN: 1471-2342. DOI: 10.1186/1471-2342-9-4. URL: <https://bmcmedimaging.biomedcentral.com/articles/10.1186/1471-2342-9-4> (visited on 10/25/2020).
- [15] Wolfgang Demtröder. *Experimentalphysik 2*. Springer-Lehrbuch. Berlin, Heidelberg: Springer Berlin Heidelberg, 2017. ISBN: 978-3-662-55789-1. DOI: 10.1007/978-3-662-55790-7. URL: <http://link.springer.com/10.1007/978-3-662-55790-7> (visited on 12/10/2020).
- [16] Jonas Philipps. *MPI pDCR Simulations*. URL: <https://git.pmi.rwth-aachen.de/jonas.philipps/ba-philipps> (visited on 01/29/2021).
- [17] Nils Holle. *MPI Simulation 1D (MPI-Matrix)*. URL: <https://git.pmi.rwth-aachen.de/nils.holle/MPI-Matrix/-/tree/master/>.

- [18] Nils Holle. *Multi-Parametric Image Reconstruction in Magnetic Particle Imaging*. 2018.
- [19] Dario Mesquida Nogueira. *Machine Learning-Based Paramter Reconstruction in Magnetic Particle Imaging*. 2020.
- [20] Dennis Pantke et al. “Multifrequency Magnetic Particle Imaging Enabled by a Combined Passive and Active Drive Field Feed-through Compensation Approach”. In: *Medical Physics* 46.9 (Sept. 2019), pp. 4077–4086. ISSN: 0094-2405, 2473-4209. DOI: 10.1002/mp.13650. URL: <https://onlinelibrary.wiley.com/doi/abs/10.1002/mp.13650> (visited on 01/31/2021).
- [21] Nils Holle. *MPI Simulation 3D*. URL: <https://uni-muenster.sciebo.de/s/6Rw1Rd6vXG0aapj> (visited on 01/26/2021).
- [22] A Weber et al. “Artifact Free Reconstruction with the System Matrix Approach by Overscanning the Field-Free-Point Trajectory in Magnetic Particle Imaging”. In: *Physics in Medicine and Biology* 61.2 (Dec. 2015), pp. 475–487. DOI: 10.1088/0031-9155/61/2/475. URL: <https://doi.org/10.1088/0031-9155/61/2/475>.
- [23] Achiya Dax. “On Row Relaxation Methods for Large Constrained Least Squares Problems”. In: *SIAM Journal on Scientific Computing* Vol. 14 (No. 3 1993), pp. 570–584.
- [24] Seyed Mohammadali Dadfar et al. “Size-Isolation of Superparamagnetic Iron Oxide Nanoparticles Improves MRI, MPI and Hyperthermia Performance”. In: *Journal of Nanobiotechnology* 18.1 (Dec. 2020), p. 22. ISSN: 1477-3155. DOI: 10.1186/s12951-020-0580-1. URL: <https://jnanobiotechnology.biomedcentral.com/articles/10.1186/s12951-020-0580-1> (visited on 01/25/2021).
- [25] micromod Partikeltechnologie GmbH. *Perimag® Magnetic Particles, Nanoparticle, Microparticles, Products*. URL: [https://www.micromod.de/en/produkte-197-magnetic\\_peri.html](https://www.micromod.de/en/produkte-197-magnetic_peri.html) (visited on 01/25/2021).
- [26] Franziska Schrank. *MPI Denoising Program*. URL: <https://git.pmi.rwth-aachen.de/franziska.schrank/mpi-denoising> (visited on 02/02/2021).